Published in final edited form as:

Cell. 2023 December 21; 186(26): 5812–5825.e21. doi:10.1016/j.cell.2023.11.009.

An enzyme that selectively S-nitrosylates proteins to regulate insulin signaling

Hua-Lin Zhou[1,2], **Zachary W. Grimmett**[2,3], **Nicholas M. Venetos**[2,4], **Colin T. Stomberski**[2,4], **Zhaoxia Qian**[1,2], **Precious McLaughlin**[1,2], **Puneet K. Bansal**[4], **Rongli Zhang**[1,2], **James D. Reynolds**[2,5,6], **Richard T. Premont**[1,2,6], **Jonathan S. Stamler**[1,2,6,†]

[1]Department of Medicine, Case Western Reserve University School of Medicine, Cleveland, OH, USA.

[2]Institute for Transformative Molecular Medicine, Case Western Reserve University School of Medicine, Cleveland, OH, USA.

[3]Department of Pathology, Case Western Reserve University School of Medicine, Cleveland, OH 44106, USA.

[4]Department of Biochemistry, Case Western Reserve University School of Medicine, Cleveland, OH 44106, USA

[5]Anesthesiology and Perioperative Medicine; Case Western Reserve University School of Medicine, Cleveland, OH, USA.

[6]Harrington Discovery Institute, University Hospitals Cleveland Medical Center, Cleveland, OH, USA

Summary

Acyl-Coenzyme A (Acyl-CoA) species are cofactors for numerous enzymes that acylate thousands of proteins. Here we describe an enzyme that uses S-nitroso-CoA (SNO-CoA) as its cofactor to S-nitrosylate multiple proteins (SNO-CoA Assisted Nitrosylase, SCAN). Separate domains in SCAN mediate SNO-CoA and substrate binding, allowing SCAN to selectively catalyze SNO transfer from SNO-CoA to SCAN to multiple protein targets, including the insulin receptor (INSR) and insulin receptor substrate 1 (IRS1). Insulin-stimulated S-nitrosylation of INSR/IRS1 by SCAN reduces insulin signaling physiologically, whereas increased SCAN activity in obesity causes INSR/IRS1 hypernitrosylation and insulin resistance. SCAN-deficient mice are thus protected

[†]lead contact and corresponding author: jonathan.stamler@case.edu.

Author contributions

Conceptualization, HLZ and JSS; Methodology, ZQ; Investigation, HLZ, ZWG, NMV, CTS, PJM, PKB, RZ; Writing, HLZ, RTP and JSS; Funding Acquisition, HLZ and JSS; Resources, JDR; Supervision, HLZ, RTP and JSS.

Conflict of interest

Jonathan Stamler is a founder and board member of and has equity interest in SNO bio, a company developing nitrosylation related therapeutics, and NNOXX, a company developing NO-based device technology. CWRU and UHCMC are aware of these conflicts and appropriate management plans are in place. None of the other authors have relevant conflicts to disclose. Discoveries herein (JSS and HZ) have been disclosed to the CWRU/UHCMC TTOs and a patent application is anticipated.

from diabetes. In human skeletal muscle and adipose tissue, SCAN expression increases with Body Mass Index and correlates with INSR S-nitrosylation. S-nitrosylation by SCAN/SNO-CoA thus defines a new enzyme class, a unique mode of receptor tyrosine kinase regulation, and a revised paradigm for NO function in physiology and disease.

Brief statement

SCAN catalyzes S-nitrosylation of proteins, including the insulin receptor (INSR) and insulin receptor substrate 1 (IRS1), to inhibit insulin signaling physiologically and cause insulin resistance in disease.

Graphical Abstract

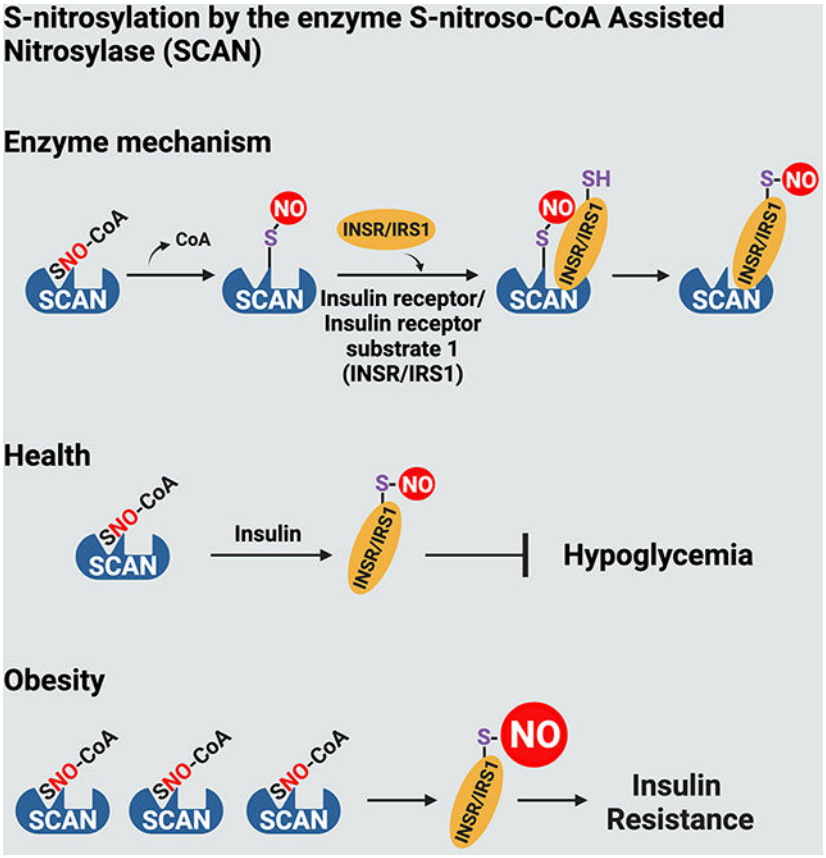

Introduction

Coenzyme A (CoA) is a cofactor for ~4% of cellular enzymes, where its reactive thiol is used to ferry biomolecule metabolites and building blocks, most prominently acetyl groups during metabolism of glucose and the synthesis of fatty acids [1,2]. CoA also has a key role in cellular signaling where it is used by enzymes to carry molecules employed for post-translational modification (PTM) of target proteins. These include most notably histone acetyltransferases (HATs) that acetylate histones and other proteins, and palmitoyl-transferases (PATs) that add palmitate or other fatty acids to proteins to regulate protein

association with cell membranes [3]. Enzymes utilizing CoA and its congeners for metabolic and signaling functions are represented by diverse structural families but share a basic mechanism in charging CoA via a thioester linkage and in transfer of acyl groups to nucleophilic substrates [4].

Coenzyme A has most recently been identified with a function in carrying endogenous nitric oxide (NO) in the form of an S-nitrosothiol (SNO; SNO-CoA)[5]. Here the thiol of CoA is uniquely activated via a thionitrite linkage (as opposed to a thioester), providing a basis for NO group transfer to target proteins in cellular signaling (aka S-nitrosylation). Thus conceived, SNO-CoA participates in a reversible chemical equilibrium with SNO-protein substrates to determine steady-state levels of cellular SNOs [5–8]. This is well-exemplified in the functions of SNO-CoA reductases (SCoRs), enzymes that degrade SNO-CoA [5,6]. Deletion of SCoRs leads to elevated SNO-CoA, thereby increasing SNO-protein levels [5,6,9]. Yet protein S-nitrosylation in this model remains exclusively non-enzymatic (i.e., SNO-CoA acts as a non-specific NO donor), and no enzymes are known to utilize SNO-CoA as a cofactor for any purpose.

As principal mediators of signal transduction, protein S-nitrosylation and phosphorylation have been suggested to share features [10], including conservation across phylogeny, global control over cellular function and site-directed modification through sequence motif recognition [10–12]. In addition, excessive or dysregulated S-nitrosylation plays causal roles in many of the same diseases as dysregulated phosphorylation, including Alzheimer's, cancers, muscular dystrophy, heart failure and diabetes [13–17]. But whereas phosphorylation of proteins is enzymatically driven, convention holds that dysregulated S-nitrosylation is mediated chemically by high amounts of NO and of LMW SNOs (like SNO-CoA) that modify proteins indiscriminately [18,19]. More recently, the idea has been raised that NO synthase-derived NO may be transferred between proteins, constituting 'nitrosylase activity', and heterotrimeric machinery for S-nitrosylation analogous to that used for ubiquitinylation has been identified in bacteria [10–12,20–25]. However, a basic catalytic mechanism that would solidify an enzymatic basis for S-nitrosylation has been elusive, and no S-nitrosylases are known to mediate physiology or disease.

Here we describe the prototype for a class of enzyme, SCAN (for SNO-CoA-Assisted Nitrosylase) that uses SNO-CoA as its cofactor to S-nitrosylate specific target proteins, and reveal core mechanistic parallels with acyltransferases, firmly establishing enzymatic function. Separate domains in SCAN are involved in SNO-CoA and target protein binding, allowing SCAN to selectively catalyze NO group transfer from SNO-CoA to SCAN to multiple target proteins, including the insulin receptor β-subunit (INSRβ) and insulin receptor substrate 1 (IRS1). SCAN activity acts physiologically to regulate insulin signaling on the one hand, while aberrant activity contributes to diabetes on the other hand. While SCAN activity is dependent on NO derived from NOS, the major role of NOS is to generate the LMW SNO cofactor. Thus, our characterization of SCAN unveils enzymatic principles shared with other enzymatic mediators of signal transduction and supports a new paradigm for NO biology.

Results

By analogy to acyltransferases that use acetyl-CoA to acetylate proteins [26], we considered that SNO-CoA might serve as cofactor for unknown nitrosylase enzymes that target S-nitrosylation of specific substrate proteins. We therefore purified SNO-CoA binding proteins from bovine liver to identify candidate SNO-CoA-dependent nitrosylases. Eight proteins that bound SNO-CoA, but not CoA, were identified (Figure 1A). Biliverdin reductase B (BLVRB) and CBR1 were the two most enriched SNO-CoA binding proteins. CBR1 is known to be a LMW SNO reductase [27]; however, the function of BLVRB is unclear. BLVRB converts fetal β-biliverdin to bilirubin during development, but retains expression in adults where its substrate is not present [28,29].

Using HEK293 cell lysates and recombinant BLVRB protein, we first confirmed that BLVRB bound SNO-CoA with relatively high affinity versus a panel of both LMW SNO- and CoA- conjugates (Figure 1B, S1A and S1B). Despite being known as an NADPH-dependent reductase enzyme [30,31], BLVRB was unable to reduce SNO-CoA (Figures S1C and S1D). To assess whether BLVRB contributed in some other manner to SNO-protein metabolism, we used SNO-protein quantitative mass spectrometry in lysates from HEK-BLVRB$^{-/-}$ cells compared with parental wild-type HEK cells (HEK-WT). We found 50 proteins whose S-nitrosylation was significantly diminished in the absence of BLVRB expression, representing potential targets of BLVRB acting as a nitrosylase (Table S1). Since protein S-nitrosylation typically operates within multiprotein complexes, we isolated the BLVRB interactome by immunoprecipitation from HEK293 cell lysates and identified 47 proteins (Table S2). Notably, six of these BLVRB-associated cytoplasmic proteins (BLVRB is mainly localized in the cytoplasm (Figures S1E and S1F)) overlapped with the BLVRB nitrosoproteome (Figure 1C), including heme oxygenase 2 (HO2), which is known to function together with BLVRB in heme metabolism [32].

In HEK293 cells or RAW 264.7 cells, HO2 was endogenously S-nitrosylated in an eNOS- or iNOS-dependent manner (Figures S2A and S2B) at two Cys sites (Cys265 and Cys282), as mutation of both Cys265 and Cys282 to arginine (HO2-C265/282R) blocked S-nitrosylation of HO2 (Figure S2C). We confirmed that BLVRB directly interacted with HO2 and this was enhanced by an NO donor (Figure S2D), and verified that S-nitrosylation of HO2 (SNO-HO2) was markedly reduced in HEK-BLVRB$^{-/-}$ cells compared with HEK-WT cells (Figures 1D and 1F). Recombinant BLVRB catalyzed S-nitrosylation of purified HO2 by SNO-CoA (Km of 13 μM), while SNO-CoA itself (in the presence of GST protein control) S-nitrosylated HO2 only at very high concentrations (Figures 1E, 1G and 1H). We conclude that BLVRB functions as a SNO-CoA-Assisted Nitrosylase (SCAN).

SNO-CoA and NADPH are structurally related (Figure S2E), and BLVDB/SCAN is a known NADPH-binding protein [33]. We investigated whether the NADPH-binding motif in SCAN might be required for SNO-CoA binding. Addition of NADPH, but not SNO-cysteamine (SNO-CoA analog), inhibited SCAN binding to SNO-CoA resin (Figure 1I) in a dose-dependent manner (Figure 1J), suggesting that NADPH and SNO-CoA share the same binding site. Although NADPH competes with SCAN binding to SNO-CoA in vitro, SCAN can utilize SNO-CoA (1μM) to S-nitrosylate HO2 in the presence of high excess

concentrations of NADPH (250 μM) or NADH (1mM) (Figures S2F–S2H), concentrations that far exceed endogenous cytosolic NADPH (3μM) or NADH (50–110μM)[34,35]. Mutation of three critical amino acids, Q14N,T15A,G16A (SCAN-QTG/NAA) within the NADPH-binding motif [33] prevented SCAN binding to SNO-CoA resin, confirming that the NADPH-binding site in SCAN is required for SNO-CoA binding (Figure 1K). Overexpression of SCAN-QTG/NAA in HEK-SCAN$^{-/-}$ cells was unable to rescue S-nitrosylation of HO2 (Figures 1L, 1M, S2I and S2J), and recombinant SCAN-QTG/NAA could not efficiently S-nitrosylate HO2 in the presence of SNO-CoA in an *in vitro* assay (Figures 1N and 1O). Thus, SNO-CoA binding to SCAN is required for SCAN-mediated S-nitrosylation of its protein substrate HO2.

To explore the mechanism of SCAN-mediated S-nitrosylation, we investigated whether SNO-Cys within SCAN is required for transnitrosylation (i.e., whether SNO-SCAN exists as an intermediate in transfer of NO groups to substrate). In HEK293 cells or RAW 264.7 cells, SCAN was endogenously S-nitrosylated in an eNOS- or iNOS-dependent manner (Figures S2K and S2L). There are two cysteine residues (C109 and C188) within SCAN. Mutation of both C188 and C109 to arginine eliminated SNO modification of SCAN (Figure 1P). SCAN-C109/188R expressed in HEK-BLVRB$^{-/-}$ cells could not rescue HO2 S-nitrosylation (Figure 1Q), and recombinant SCAN-C109/188R cannot S-nitrosylate the substrate HO2 in vitro (Figure 1R and 1S), indicating that SNO-SCAN is required for S-nitrosylation of HO2. To investigate if interaction between BLVRB and substrate HO2 is required for BLVRB-mediated S-nitrosylation, we generated a truncated HO2 protein (HO2-195-316), which retains the two SNO sites (Cys265/282), but is unable to interact with BLVRB (Figures S2M and S2N). In vitro assays indicated that BLVRB/SCAN cannot efficiently nitrosylate HO2-195-316 (Figure S2O). These results suggest that SCAN utilizes a ‘ping-pong’ mechanism to catalyze S-nitrosylation. SCAN associates with both SNO-CoA and HO2 substrate; NO groups are then transferred from SNO-CoA to SCAN-C109/188 (forming SNO-SCAN), and from SNO-SCAN to the substrate (Figure 1T), yielding product (SNO-HO2).

To investigate the physiological role of SCAN in mammals, we utilized global SCAN-knockout mice (SCAN$^{-/-}$) (Figures 2A and S3A). The level of bilirubin in serum and whole blood cell counts are indistinguishable in SCAN$^{-/-}$ and wild-type mice (SCAN$^{+/+}$), confirming that BLVRB/SCAN is not involved in biliverdin degradation or hematopoiesis in adult mice under normal conditions (Figures S3B–S3F)[36]. Because insulin receptor substrate 4 (IRS4), the IRS family member predominantly expressed in HEK293 cells, was identified in the SCAN-dependent nitrosoproteome (Figure 1C), and because SCAN contains an insulin receptor (INSR)-interacting motif with unknown function [37], we explored a role for SCAN/SNO-CoA in insulin signaling.

We first confirmed that SCAN interacts with both INSR and IRS1 and found that interactions are greatly increased by NO donor treatment or insulin stimulation (Figures S4A–S4C). Mutation of the SCAN SNO-CoA binding site (QTG/NAA) or its SNO sites (C109/188R) reduced the association of SCAN with the INSR (Figure S4D), consistent with a ping-pong mechanism (Figure 1T). Expression of SCAN was dramatically increased in skeletal muscle from 12-week-old genetically obese mice (ob/ob) and from wildtype

mice fed a high fat diet (HFD) for 12 weeks and was paralleled by increases in iNOS expression (Figure 2B). $SCAN^{-/-}$ mice gained weight more slowly than $SCAN^{+/+}$ mice on HFD (Figure S4E). $SCAN^{-/-}$ mice fed a HFD for 16-weeks displayed reduced blood glucose after 5-hours of fasting, compared to $SCAN^{+/+}$ mice (Figure 2C), but blood insulin levels were normal (Figure 2D), indicating that insulin signaling, not pancreatic insulin production/secretion, is responsible for protection from hyperglycemia. Insulin tolerance tests showed higher sensitivity to insulin in HFD-fed $SCAN^{-/-}$ mice than in $SCAN^{+/+}$ mice (Figure 2E). Although basal glucose levels are much lower in HFD-fed $SCAN^{-/-}$ mice than WT, glucose tolerance tests demonstrated a similar pattern in glucose uptake between HFD-fed $SCAN^{+/+}$ and $SCAN^{-/-}$ mice (Figure 2F), which may reflect elevated insulin levels in HFD-fed WT mice (Figure 2D). That is, higher insulin levels may alleviate glucose intolerance in WT mice resulting from hyper-S-nitrosylation of IRS1/INSR. Using the ^{14}C-labeled non-metabolizable glucose analog 2-deoxyglucose as a tracer, we found that knockout of SCAN in HFD-fed mice improved insulin-stimulated glucose transport in *ex vivo* soleus muscle (Figure 2G). Therefore, SCAN contributes to insulin resistance in HFD-obese mice, whereas SCAN deletion improves insulin sensitivity.

Excessive S-nitrosylation of INSRβ/IRS1 by iNOS-derived NO is implicated in insulin resistance and provides a model for pathological S-nitrosylation in disease [38,39]. In this model, S-nitrosylation was proposed to be mediated chemically by high amounts of reactive NO. Thus, we sought to determine if S-nitrosylation of INSRβ/IRS1 is in fact mediated enzymatically by SCAN/SNO-CoA. Amounts of SNO-INSRβ and SNO-IRS1 were much higher in skeletal muscle of HFD- or chow-fed WT mice than in $SCAN^{-/-}$ mice (Figures 2H and 2I). Further, amounts of SNO-INSRβ and SNO-IRS1 were higher in HFD- than chow-fed WT mice, but diet had no effect on SNO-levels in $SCAN^{-/-}$ mice. Thus, SCAN is required for S-nitrosylation of INSRβ and IRS1 in situ. Further, in in vitro assays, purified SCAN efficiently S-nitrosylated purified INSR and IRS1 (Km of 0.96 μM and 4.57 μM, respectively) (Figures 2J, 2K and S4F–S4H). To investigate the role of SNO-CoA per se in S-nitrosylation of INSR/IRS1, we utilized SNO-CoA reductase (SCoR) knockout mice and cells, which cannot effectively metabolize SNO-CoA. Both SCoR and SCAN are localized mainly in the cytoplasm (Figure S5A). Deletion of SCoR in HEK cells increased association of SCAN with INSRβ (Figure S5B). High-fat diet fed SCoR-knockout mice ($SCoR^{-/-}$) demonstrated increased S-nitrosylation of INSRβ/IRS1 and reduced phosphorylation of the insulin effectors AKT and AS160 (Figures S5C–S5F). Taken together, our data support the notion that S-nitrosylation of INSRβ and IRS1 is enzymatically mediated, and that hypernitrosylation of proteins after iNOS induction may require SCAN and SNO-CoA.

To determine if SCAN-mediated S-nitrosylation of INSRβ/IRS1 regulates insulin signaling, we measured the phosphorylation of INSRβ, IRS1, AKT and AS160 in skeletal muscle of HFD-fed mice after intraperitoneal injection of insulin. The insulin-stimulated phosphorylation levels of INSRβ(Tyr1162), IRS1(Tyr608), AKT(Ser473) and AS160(Thr642) were all higher in $SCAN^{-/-}$ mice than $SCAN^{+/+}$ mice, indicating that S-nitrosylation by SCAN inhibits INSRβ/IRS1-dependent insulin signaling, at least in significant part through inhibition of tyrosine kinase activity of INSRβ (Figures 2L and S5G).

To further explore the physiological role of SCAN-mediated inhibition of insulin signaling, we generated SCAN-deficient rat myoblast L6 cell lines (L6-SCAN$^{-/-}$) (Figure S5H). While L6-SCAN$^{-/-}$ cells and wild-type parental L6 cells (L6-WT) have similarly low basal levels of SNO-INSRβ and SNO-IRS1, insulin increased S-nitrosylation of INSRβ/IRS1 in L6-WT cells, but not in L6-SCAN$^{-/-}$ cells. Insulin-stimulated S-nitrosylation of INSRβ/IRS1 was dynamic in L6-WT cells, reaching a peak 60–120 min after removal of insulin (after a 10-minute treatment), and gradually subsiding (Figures 3A–3C). Similarly, intraperitoneal insulin injection in chow-fed SCAN$^{+/+}$ mice induced significant S-nitrosylation of INSRβ/IRS1, but not in SCAN$^{-/-}$ mice (Figures 3D and 3E). We investigated the function of insulin-induced S-nitrosylation of INSRβ/IRS1 in L6 cells and in healthy mice. We found that deletion of SCAN in L6 cells prolongs insulin-stimulated phosphorylation of IRS1, AKT and AS160 (Figures 3F and S5I–S5L). This suggests that agonist-stimulated S-nitrosylation of INSRβ/IRS1 is part of a negative feedback loop that turns off insulin signaling. To validate this idea in mammals, we performed an insulin tolerance test in chow-fed SCAN$^{+/+}$ and SCAN$^{-/-}$ mice. Recovery of glucose levels after insulin injection (1 U/kg or 2.5 U/kg) was delayed in SCAN$^{-/-}$ mice compared to SCAN$^{+/+}$ mice (Figures 3G and 3H), consistent with higher S-nitrosylation of INSRβ in SCAN$^{+/+}$ than in SCAN$^{-/-}$ skeletal muscle (Figure 3I and 3J). These results confirm that insulin-induced S-nitrosylation mediated by SCAN acts to turn off insulin signaling in skeletal muscle, thereby slowing glucose uptake to prevent hypoglycemia.

Insulin treatment in both WT mice and L6-WT cells markedly increased phosphorylation of eNOS at Ser1177 and nNOS at Ser1412, respective measures of eNOS and nNOS activity (Figures 4A–4F and S5M) [40]. Taken together, our results indicate that SCAN mediates insulin-stimulated S-nitrosylation of INSRβ/IRS1 in both L6 cells and skeletal muscle of healthy mice, likely using NO generated by eNOS or nNOS (Figures S5N and S5O). This was confirmed by showing that in L6 cells, the NOS inhibitor L-NMMA blocked insulin stimulated S-nitrosylation not only of INSRβ and IRS1 but also of SCAN itself (Figures 4G–4J). Accordingly, phosphorylation of AKT and AS160 was increased in the presence of L-NMMA (Figures 4K, S5P and S5Q). Thus, eNOS and nNOS may provide the source of SNO for SCAN activity under physiological conditions.

As a confirmatory measure, we re-expressed SCAN-WT (L6-SCAN-WT), the SCAN-QTG/NAA mutant unable to bind SNO-CoA (L6-SCAN-QTG/NAA) or the SCAN-C109/188R mutant unable to form SNO (L6-SCAN-C109/188R) in SCAN-deficient rat myoblast L6 cell lines (L6-SCAN$^{-/-}$) (Figure S6A). Re-expression of SCAN-WT, but not SCAN-QTG/NAA or L6-SCAN-C109/188R, rescued the S-nitrosylation of INSRβ and IRS1, and inhibited insulin-stimulated phosphorylation of IRS1 and AKT (Figures 5A–5D). Thus, the S-nitrosylation of INSRβ/IRS1 and subsequent inhibition of insulin signaling requires SCAN and SNO-CoA. To dissect the role SNO-INSRβ in insulin signaling, we first mapped the SNO sites in INSR. Four peptides containing four candidate Cys SNO sites were identified (Figure 5E); Cys825, Cys834 and Cys1083 are present in INSRβ, while Cys462 is in INSRα. Using mutagenesis, we determined that Cys1083 is the primary SNO site in INSRβ; in HEK293 cells, mutation of Cys1083 to Ala (INSR-C1083A) reduced the S-nitrosylation of INSRβ by ~70% (Figures 5F and 5G). The INSRβ SNO-site (Cys1083) is localized in the tyrosine kinase catalytic domain (IRK). Insulin-stimulated IRK cross-

phosphorylates the activation loop of the other INSR in the dimer, triggering its intrinsic tyrosine kinase activity [41]. Using Pymol, we determined that the SNO-site Cys1083 resides at the interface between two IRKs of dimeric INSR, suggesting that S-nitrosylation may affect cross-phosphorylation (Figure S6B). To investigate the role of INSR-C1083A in insulin signaling, endogenous INSR in L6 cells was deleted and then replaced by INSR-WT or INSR-C1083A (Figures S6C and S6D). Following stimulation with insulin, cells expressing mutant receptor refractory to S-nitrosylation (INSR-C1083A) showed increased and sustained phosphorylation of AKT and AS160 (vs. WT INSR) (Figures 5H–5J). Thus, SCAN turns off insulin signaling by S-nitrosylation of INSRβ. SNO-INSRβ may be considered a marker of insulin receptor desensitization.

To determine if S-nitrosylation of INSRβ by SCAN is involved in obesity-related insulin resistance in humans, we quantified the expression of SCAN and amount of SNO-INSRβ in 14 human skeletal muscle samples and in 26 human adipose depot samples from patients with a range of Body Mass Index (BMI) (Table S3). Notably, we found that expression of SCAN is upregulated in both skeletal muscle and in visceral and subcutaneous adipose samples from patients with higher BMI (Figures 6A–6C, S6E and S6F). A significant linear relationship between the amount of SNO-INSRβ and BMI in human tissues suggests that S-nitrosylation of INSRβ is an important factor in insulin resistance in humans (Figures 6D–6F, S6G and S6H). Further, a significant linear correlation between amounts of SNO-INSRβ and the expression of SCAN protein in both human skeletal muscle and human adipose tissues (Figures 6G and 6H) implies that S-nitrosylation of INSRβ is likely mediated by SCAN in human tissues. Collectively, the multiple linear correlations among SCAN expression, BMI, and SNO-INSRβ (taken together with animal data), suggests that overexpression of SCAN in obese patients contributes to insulin resistance through hypernitrosylation of INSRβ.

INSRβ is one of multiple receptor tyrosine kinases (RTKs) that have been reported to be S-nitrosylated, including insulin-like growth factor 1 receptor (IGF-1) and epidermal growth factor receptor (EGFR), and our survey of papers reporting SNO-protein identification from untargeted mass spectroscopy identified 20 of the 58 RTK family members as S-nitrosylated (Table S4) [42–45]. We find that four additional RTKs (FGFR1, PDGFRβ, VEGFR2 and HER3) are S-nitrosylated in human HEK293 cells (Figures S6I–S6K). S-nitrosylation of other RTKs by additional SCAN-like enzymes therefore seems likely.

Discussion

It is predicted that 70% of the entire proteome is subject to S-nitrosylation and over 10,000 SNO-proteins have been identified [46,47]. Accumulating evidence suggests that S-nitrosylation is site-specific and enzymatically regulated, entailing enzymes that produce NO, generate SNO from NO, and transfer SNO to target proteins [11,12,21,22]. In addition, multiple enzymes can eliminate SNO [5,6,48,49]. Nonetheless, our understanding of basic catalytic mechanisms of S-nitrosylation remains rudimentary, and unifying features that would define enzyme families by analogy to kinases, acetyltransferases and ubiquitin ligases have remained elusive. Thus, it is still widely believed that S-nitrosylation is primarily non-enzymatic [18,50] i.e., mediated chemically by NO and related congeners.

SCAN changes this paradigm by defining an enzymatic mechanism utilizing SNO-CoA that draws clear parallels to acyltransferases with their acyl-CoA cofactor [3]. SCAN function is also instructive because physiological activity is stimulus-coupled via the insulin receptor tyrosine kinase, while aberrant activity causes disease, paralleling phosphorylation. These data argue strongly for enzymatic S-nitrosylation as a principal mechanism of signal transduction and define a nitrosylase class based on catalytic mechanism.

Protein dependent S-nitrosylation has been convincingly demonstrated for multiple SNO-proteins including hemoglobin, GAPDH, thioredoxin and S100A8/A9 [12,22,23,25,51] However, strict enzymatic criteria (that would justify a 'nitrosylase' designation) have not been met previously, as these SNO-proteins are consumed in a single reaction cycle that generates product (whereas a catalyst is not consumed in a chemical reaction). Thus, the concepts of catalyst and substrate are blended. By contrast, SCAN fully meets enzymatic criteria, including demonstrated specificity, catalytic activity, and conversion of substrate to product. SCAN thus turns over in vitro with classic enzyme kinetics. Moreover, SCAN reveals a unifying catalytic mechanism for transnitrosylases entailing NO group transfer chemistry from SNO-substrate (e.g. SNO-CoA) to SNO-product (e.g., SNO-INSR, SNO-IRS, SNO-HO2), and suggests at least 2 classes of transnitrosylases based on source of SNO: LMW-SNO (as in SCAN) and Protein-SNO (as in GAPDH), where a dedicated SNO synthase provides the SNO-substrate, as shown in E. coli [21].

Given that multiple proteins bind to SNO-CoA resin (Figure 1A) and many of these (e.g., ACADVL, ALDH, ACADS, GLYAT) contain a binding domain for cosubstrates or cofactors (NADPH, FAD, or acetyl-CoA) that share structure with SNO-CoA, it seems likely that additional SCAN-like enzymes exist, by analogy to the multiple acetyl-CoA dependent acetyltransferase family members. Thus, multiple nitrosylases may utilize SNO-CoA cofactor, while other endogenous LMW SNOs, including GSNO and CysNO, may act as cofactors for additional classes of nitrosylases. Our findings thus fundamentally revise the conception of LMW SNO action, from being only nonspecific NO donors to acting as specific enzyme cofactors. More broadly, SCAN activity can be understood in terms of a catalytic mechanism shared by HATs, PATs and ubiquitin ligases: group transfer chemistry from activated thiyl-donors (thionitrites and thioesters) to target nucleophiles, including cysteine and lysine. Particularly, SCAN utilizes a 'ping-pong' mechanism to catalyze S-nitrosylation. The NO group is first transferred from SNO-CoA to SCAN, and then from S-nitrosylated SCAN to its substrate; therefore, SCAN may only require transient binding to SNO-CoA to induce SCAN auto-S-nitrosylation. This may help explain why SNO-CoA can compete with endogenous NADPH to efficiently nitrosylate substrates (despite sharing a binding site in SCAN). By the same token, our results refine the mechanism of disease caused by S-nitrosylation from that of excessive NO (e.g., derived from iNOS) modifying proteins indiscriminately to that of dedicated enzymes directing elevated NO to specific targets just as they do at normal levels of NO (e.g., from eNOS). It should be noted in this regard that the hyper-S-nitrosylation of proteins that is known to be causal in insulin resistance, is also an established feature of other diseases including heart failure, Alzheimer's disease, muscular dystrophy, malignant hyperthermia and liver cancer [15,17,52,53]. SCAN-like enzymes may therefore represent attractive therapeutic targets in many diseases.

We have identified SCAN activity as residing in the fetal biliverdin reductase protein (BLVRB). There are two non-redundant biliverdin reductases in mammals (BLVRA and BLVRB), which can respectively convert two types of isomeric biliverdins (adult α-biliverdin and fetal β-biliverdin) to bilirubin. The fetal β-biliverdin substrate is lacking in adults, yet BLVRB remains expressed in adult tissues [33,54] where it has been implicated in hematopoiesis [36,55], intermediary metabolism (glutaminolysis, glycolysis, TCA cycle and pentose phosphate pathway), and cholangiocarcinoma cell motility by inhibiting the Notch/Snail signaling pathway [56,57]. BLVRB has been identified as a non-specific flavin reductase [58], but this activity is not linked to physiological functions or targets and the mechanism of BLVRB action has remained a mystery [28,36]. Our work thus raises the possibility of enzymatic roles for S-nitrosylation in metabolic regulation, erythropoiesis and cancer.

In addition to biliverdin reductase activity required for heme degradation, adult BLVRA is a serine/threonine kinase involved in the negative feedback regulation of insulin signaling. BLVRA is activated by the tyrosine kinase activity of the insulin receptor, and then phosphorylates IRS1 to inhibit insulin action [59]. Liver-specific knockout of BLVRA in obese mice has been associated with glucose/insulin alterations and fatty liver disease [60]. Interestingly, BLVRB also has the insulin receptor interaction motif, but does not have protein kinase activity [28]. Here we show that BLVRB is a protein S-nitrosylase that regulates the insulin pathway via S-nitrosylation of INSRβ and IRS1. Thus remarkably, both members of the BLVR family have enzymatic function to regulate the insulin pathway, but via distinct post-translational modifications: phosphorylation mediated by BLVRA and S-nitrosylation mediated by BLVRB/SCAN.

eNOS in skeletal muscle is required for normal insulin responsiveness [61,62]. By contrast, iNOS-derived NO is deleterious to insulin signaling and contributes to the pathophysiology of T2DM [63,64]. Thus, NO can mediate both beneficial and deleterious effects on insulin signaling. Our studies provide context and mechanism for these opposing effects. In healthy conditions, insulin stimulation of its receptor is coupled to eNOS/nNOS mediated S-nitrosylation of INSRβ/IRS1, which terminates physiological insulin signaling to avoid hypoglycemia. However, in obesity, iNOS is induced by pro-inflammatory cytokines in skeletal muscle, uncoupling NO generation from insulin signaling. This results in hyper-S-nitrosylation of INSRβ/IRS1 and leads to insulin resistance (Figure 6I). Importantly, NOS activity is necessary but not sufficient for S-nitrosylation, as NO itself cannot chemically S-nitrosylate proteins [65]. Rather, S-nitrosylation is routed through SNO-CoA by the enzymes SCAN and SCoR, which together determine steady state levels of SNO-INSRβ/IRS1, by analogy to a kinase/phosphatase pair.

The insulin receptor is a member of the receptor tyrosine kinase (RTK) family of 58 cell surface receptors for growth factors, cytokines, and hormones [66]. We reveal many RTKs to be S-nitrosylated, implying a class effect with shared regulatory mechanisms (Figure S6 and Table S4). Thus, our finding of insulin induced S-nitrosylation of INSRβ/IRS1 in healthy tissues, and hypernitrosylation of INSRβ/IRS1 in diabetes, may provide a working model for enzymatic S-nitrosylation in health and disease (Figure 6I): In physiological situations, nitrosylase-catalyzed S-nitrosylation is induced by agonists to regulate cellular signaling. In disease, S-nitrosylation is dysregulated or disrupted by aberrant nitrosylase activity, possibly

uncoupled from receptor stimulation. These findings suggest therapeutic opportunities that extend to the human condition. Collectively, our studies provide insights into obesity-linked diabetes mellitus, raise the tantalizing idea that RTKs may be feedback-regulated by SCAN or similar enzymes, and suggest a revised paradigm for NO biology in health and disease.

Limitations of the Study

While the SNO-RAC-coupled western blot method for S-nitrosylation is amenable to calculating Km of SCAN, it is not suitable for calculating Kcat because of its low efficiency. Formally, SNO-CoA is a cosubstrate in the enzymatic reaction catalyzed by SCAN. For ease of understanding, we describe SNO-CoA as a cofactor (broader term). We used mice with constitutively deleted SCAN, so we cannot distinguish the role of S-nitrosylation of INSR and IRS1 mediated by SNO-CoA/SCAN within specific organs or tissues, such as liver, adipose and skeletal muscle. The human data overall are supportive of associations among SCAN level and BMI/SNO-INSR, but these correlations will benefit from further validation in a larger number of samples (particularly at higher BMI).

STAR Methods

RESOURCE AVAILABILITY

Lead contact

- Further information and requests for resources and reagents should be directed to and will be fulfilled by the lead contact, Jonathan Stamler (jss156@case.edu).

Materials availability

- Plasmids and other reagents generated in this study are available from the lead contact upon reasonable request.

Data and code availability

- Original western blot images have been deposited at Mendeley Data and are publicly available as of the date of publication. The DOIs are listed in the key resources table.
- No original code was generated in this project.
- Any additional information required to reanalyze the data reported in this paper is available from the lead contact upon request.

Experimental Model and Study Participant Details

Mice—Mouse studies were approved by the Case Western Reserve University Institutional Animal Care and Use Committee (IACUC). Housing and procedures complied with the Guide for the Care and Use of Laboratory Animals and with the American Veterinary Medical Association Guidelines on Euthanasia. All mice were housed in a specific pathogen-free barrier facility on a 12:12 light:dark cycle with ad libitum access to food and water. The standard chow diet was Teklad P3000 (Envigo).

SCAN$^{+/-}$ mice were generated by Model Animal Research Center, Nanjing University. Briefly, the inactivated *Blvrb* allele in ES cells was first created by insertion of a LacZ-Neo cassette in place of exons 2, 3 and 4 of the *Blvrb* gene, disrupting in-frame translation of BLVRB (Figure S3A) [67]. Targeted ES cells were injected into blastocysts to generate chimeric mice, and male chimeras were bred to C57BL/6J females to produce BLVRB$^{+/-}$ F1 mice. BLVRB$^{+/-}$ F1 males and females were used as breeders to generate control mice (BLVRB$^{+/+}$) and homozygous mutant mice (BLVRB$^{-/-}$), which were maintained by intercrossing BLVRB$^{+/+}$ males and BLVRB$^{+/+}$ females or BLVRB$^{-/-}$ males and BLVRB$^{-/-}$ females, respectively. Genotyping of *Blvrb* used the following PCR primers: Blvrb-FRT-tF1 5'AGAGTTTGGGTCCTCCCTTTCCT3' and common-En2-R: 5'CCAACTGACCTTGGGCAAGAACAT3'.

To induce dietary obesity, 6–7-week-old male mice (body weight: 20–23g) were fed high-fat diet (60 kcal% fat diet D12492, Research Diets, Inc.) for 16 weeks before use in experiments.

Male *ob/ob* mice (Jax #000632), homozygous for the obese spontaneous mutation, were purchased from Jackson Labs and fed standard chow diet for 16 weeks before use in experiments.

Cell culture and generation of CRISPR-knockout and replacement cell lines.—HEK293 and L6 cells were obtained from ATCC and cultured according to the ATCC protocols at 37°C under 5% CO_2 in complete DMEM (10% FBS, 1% Pen-Strep). To induce the production of nitric oxide in HEK293 cells, pcDNA-eNOS was co-transfected into HEK293 cells using PolyJet transfection reagent. HEK-BLVRB knockout cell lines (HEK-BLVRB$^{-/-}$), L6-SCAN knockout cell lines (L6-SCAN$^{-/-}$), and L6-INSR knockout cell lines (L6-INSR$^{-/-}$) were created using CRISPR-Cas9 with specific guide RNAs. The human BLVRB CRISPR/Cas9 KO plasmid and BLVRB HDR plasmid were from Santa Cruz Biotechnology; the rat eSpCas9-rBLVRB and eSpCas9-rINSR plasmids were from GenScript. The eSpCas9-rSCAN contained gRNAs 5'-CCCCTCTGACGGTAACCTGC-3' and 5'-TCGGTGCCACCGGAAGGACC-3' targeting rat BLVRB gene. The eSpCas9-rINSR plasmids contained gRNAs 5'-TATCGACTGGTCCCGCATCCTGG-3' and 5'-GCCTGATTATCAACATCCGAGGG-3' targeting rat INSR gene. HEK-293 or L6 cells were transfected with BLVRB CRISPR/Cas9 KO /BLVRB HDR plasmid, eSpCas9-rBLVRB or eSpCas9-rINSR using PolyJet transfection reagent per manufacturer's instructions. Twenty-four hours after transfection, the media was replaced, and cells were grown for another 24 hours. Cells were then split into growth media. After 48 hours, media containing 3 μg/mL puromycin was added to select for candidate knockout cell colonies. Single colonies were picked and cultured in 96-well plates with growth media containing 3 μg/mL puromycin. Knockout cell lines were confirmed by western blot. Puromycin-resistant colonies containing normal endogenous expression of BLVRB (or INSR) were used for negative controls. To build stable HEK-BLVRB-WT, BLVRB-QTG/NAA, L6-SCAN-WT and L6-SCAN-QTG/NAA cell lines, HEK-BLVRB$^{-/-}$ or L6-SCAN$^{-/-}$ knockout cells were transfected with pcDNA-hBLVRB-WT or pcDNA-hBLVRB-QTG/NAA using PolyJet transfection reagent per manufacturer's instructions. To build stable L6-INSR-WT and L6-INSR-C1083 cell lines, L6-INSR$^{-/-}$ were transfected with pcDNA-hINSR-WT or pcDNA-

hINSR-C1083. Twenty-four hours after transfection, media was changed and cells grown for another 24 hours before being split into growth media. After 48 hours, G418 was added into the media at 400 μg/mL to select for cell lines expressing the proteins of interest. Expression in the stable cell lines was confirmed by western blot.

Human Samples—Acquisition of deidentified human skeletal muscle samples, human visceral adipose and human subcutaneous adipose tissue samples was approved by the Institutional Review Board (IRB) for the protection of human subjects at Case Western Reserve University under a protocol waiver.

Deidentified frozen human samples with pathological characterization were provided by the Tissue Resource Core at University Hospitals Cleveland. Human tissue was snap-frozen in liquid nitrogen immediately after collection from surgical procedures. Information of patient's age, sex, race, BMI and type of tissue was obtained from pathology reports, and are provided in Table S3. Average age of patients for adipose tissues is 55.3 ± 13.4 years (ranging from 34 to 87 years). Average age of patients for skeletal muscle is 61.2 ± 12.6 years (ranging from 37 to 85 years). The SCAN expression and SNO levels of INSR in human samples were quantified by semi-quantitative analysis from western blots. SCAN expression was normalized relative to GAPDH detected on the same gel to control for any variation of protein loading among samples. These values were then normalized to the mean value (mean for all samples in same gel) for each gel to create a normalized measure to allow samples from two replicate gels to be directly compared.

METHOD DETAILS

Plasmids, Cloning and Mutagenesis—Human cDNA of HO2 and cDNA of SCAN were cloned through reverse transcriptase–polymerase chain reaction (RT-PCR). The mammalian cell expression plasmids pCS2-flag-hHO2 and pcDNA-myc-hSCAN were generated through inserting cDNA of HO2 and SCAN into vector pCS2-flag and pcDNA3.1-myc, respectively. The pcDNA-flag-hIRS1 and pcDNA-flag-hINSR were obtained from GenScript. pCS2-flag-hHO2-C127R, pCS2-flag-hHO2-C265R, pCS2-flag-hHO2-C282R, pcDNA-myc-hSCAN-QTG/NAA, pcDNA-myc-hSCAN-C109R, pcDNA-myc-hSCAN-C188R and pcDNA-myc-hSCAN-C109/188R, pcDNA-flag-hINSR-C825A, pcDNA-flag-hINSR-C834A and pcDNA-flag-hINSR-C1083 mutants were generated by QuikChange II Site-Directed Mutagenesis Kit (Agilent). The mammalian cell expression plasmids containing truncated hHO2(1–296), hHO2(65–316), hHO2(130–316) or hHO2(195–316) were generated subcloning PCR bands of HO2 truncations into pCS2-flag. Primers are listed in Table S5. For purification of recombinant hHO2, hHO2(195–316), hSCAN-WT or hSCAN-QTG/NAA and hSCAN-C109/188R, cDNA encoding human HO2, hHO2(195–316), SCAN-WT, SCAN-QTG/NAA and hSCAN-C109/188R gene were subcloned into the pET21b vector to introduce a C-terminal 6xHis tag on the expressed protein. FGFR1 in pDONR221 vector was purchased from DNASU. All others (VEGFR2/KDR #23925, PDGFRa #23892, PDGFRb #23893, HER3 #23874) in pDONR223 vector were purchased from Addgene. These entry vectors were cloned into pcDNA-DEST40 Gateway destination vectors (Invitrogen) using Gateway LR clonase II

reaction, generating mammalian expression plasmids with terminal V5 tag. All plasmids and mutations were confirmed by DNA sequencing.

SNO-CoA agarose bead pull down—Coenzyme A–agarose (50% slurry) was prepared by suspending Coenzyme A–agarose powder (Sigma) in water overnight at 4°C. To generate SNO-CoA beads, CoA beads were washed twice with 30 volumes of 10 mM HCl and supernatant was aspirated. Pelleted CoA beads were resuspended in 0.5 ml of 10 mM HCl, and 0.5 ml of 10 mM $NaNO_2$ was added to the suspension to generate SNO-CoA. Immediately following $NaNO_2$ addition, 10 ml of washing buffer (150 mM NaCl, 1 mM EDTA, 1 mM DPTA, 0.1 mM neocuproine (Sigma) and 50 mM borate buffer, pH 8.0) was added to dilute the SNO-CoA beads. The SNO-CoA beads were washed three times with washing buffer. For pulldown experiments, bovine liver tissue (5g) was suspended in 25 mL of lysis buffer (150 mM NaCl, 1 mM EDTA, 1 mM DPTA, 0.1 mM neocuproine, 50 mM borate buffer, pH 8.0, 1 mM PMSF and protease inhibitor mixture) and lysed in a blender, followed by homogenization with a Dounce homogenizer (Wheaton). Following centrifugation twice at 60,000 × g for 45 min, the supernatant was collected. The low-molecular weight cofactor NADPH was removed from the lysate using Amicon Ultra 3K Centrifugal Filter Devices. To pre-clear the CoA-binding proteins in the lysate, 10 ml of lysate (30 mg/ml) was incubated with 0.3 ml CoA–agarose beads for 2 hours in the cold room in the dark. The pre-cleared lysate was incubated with 0.1 ml SNO-CoA beads for 2 hours at 4°C in the dark. After incubation, the beads were washed six times with washing buffer (150 mM NaCl, 1 mM EDTA, 1 mM DPTA, 0.1 mM neocuproine, and 50 mM borate buffer, pH 8.0), and SNO-CoA-binding proteins were eluted with excess SNO-CoA (20 mM, prepared as for SNO-CoA beads).

For in vitro binding experiments, 1 μg of recombinant BLVRB protein diluted in 1 ml of binding buffer (150 mM NaCl, 1 mM EDTA, 1 mM DPTA, 0.1 mM neocuproine, and 50 mM borate buffer, pH 8.0) was incubated with 30 μl of 50% amylose resin (BioLabs), activated thiol Sepharose 4B (Cytiva GE Healthcare), thiopropyl Sepharose 6B (GE healthcare), glutathione–agarose (Invitrogen), SNO-modified activated thiol (GSNO)–Sepharose 4B, SNO-CoA–agarose or CoA–agarose for 2 hours at 4°C in the dark. For in vivo binding experiments, 1 ml of HEK cell lysate (1 mg/ml) was incubated with 30 μl of 50% GSH–agarose, GSNO–Sepharose 4B, CoA–agarose, Acetyl-CoA–agarose, SNO-CoA–agarose or Palmitoyl-Coenzyme A–agarose (Sigma) for 2 hours at 4°C in the dark. Beads were washed six times with binding buffer, and bound proteins were eluted with 50 μl of 1X SDS loading dye (Invitrogen) containing 5% 2-mercaptoethanol (Sigma).

SNO-RAC—SNO-RAC was carried out as described previously [52]. Mouse skeletal muscle and human skeletal muscle were manually homogenized in liquid nitrogen with mortar and pestle. Ground skeletal muscle or human adipose tissue were homogenized in lysis buffer (1 mg/5 μl lysis buffer) containing 100 mM Hepes, 1 mM EDTA, 100 μM neocuproine (HEN), 50 mM NaCl, 0.1% (vol/vol) Nonidet P-40, 0.2% S-methylmethanethiosulfonate (MMTS) as a free thiol-blocking agent, 1 mM PMSF and protease inhibitors using Beadbeater (BioSpec). After centrifugation (20,000 × g, 4 °C, 20 min, ×2), SDS and MMTS were added to the supernatants to 2.5% and 0.2% respectively, and incubated at 50°C for 20

min. Proteins were precipitated with −20°C acetone, and re-dissolved in 1 mL of HEN, 1% SDS. Precipitation of proteins were repeated with −20°C acetone and the final pellets were resuspended in HEN, 1% SDS buffer, and protein concentrations were determined using the Bicinchoninic Acid (BCA) method. Total lysates (2 mg) were incubated with freshly prepared 50 mM ascorbate and 50 μl thiopropyl-Sepharose (50% slurry) and rotated end-over-end in the dark for 4 h. The bound SNO-proteins were sequentially washed with HEN, 1% SDS and then 10% HEN, 0.1% SDS buffers; SNO-proteins were eluted with 10% HEN, 1% SDS, 10% β-meracaptoethanol and analyzed by SDS/PAGE and immunoblotting.

In vitro S-nitrosylation assay—For in vitro assay of S-nitrosylation of HO2, two master tubes were prepared. The control reaction tube contained 5 μg of HO2–6xHis, 5 μg GST and 2000 μL assay buffer (phosphate buffer pH 7.0 supplemented with 100 μM EDTA, 100 μM DTPA and 0.1% NP-40). The enzyme reaction tube contained 5 μg of HO2–6xHis, 5 μg SCAN and 2000 μL assay buffer. The master mixture was separated into 5 tubes (400 μl/tube). 20 μl of SNO-CoA dilutions (0, 2 μM, 20 μM, 200 μM or 2 mM) were added into pairs of control and enzyme tubes.

For in vitro assay of S-nitrosylation of HO2 mediated by mutant SCAN, two master tubes were prepared. The control reaction tube contained 4 μg of HO2–6xHis, 4 μg GST and 1600 μL assay buffer. The enzyme reaction tube contained 4 μg of HO2–6xHis, 4 μg SCAN-QTG/NAA, SCAN-C109/188R and 1600 μL assay buffer. Master mixture was split into 4 assay tubes (400μl/each tube), and 20μl SNO-CoA dilutions were added into individual tubes to final concentrations of 0, 20 μM, 200 μM or 2 mM. For in vitro S-nitrosylation of IRS1 and INSR, two master tubes were prepared. Control reaction tube contained 1 μg of IRS1-FLAG or 1 μg of INSR-FLAG, 5 μg GST and 2000 μL assay buffer. Enzyme reaction tube contained 1 μg IRS1-FLAG or 1 μg INSR-FLAG, 5 μg SCAN and 2000 μL assay buffer. The master mixture was equally separated into 5 tubes (400 μl/each tube). 20 μl SNO-CoA (0, 20 μM, 200 μM, 2 mM or 4 mM) was respectively added into the tubes. Reaction tubes were incubated at 37°C for 30 minutes in the dark. Reactions were quenched by the addition of 3 volumes ice cold 100% acetone. Following quenching, 50 μL 2 μg/μL BSA was added to samples. Proteins were precipitated at −20°C for 30 minutes, pelleted at 4500 g for 8 minutes, and washed 4X with 70% acetone. Protein pellets were resuspended in 300 μL HEN buffer containing 2.5% SDS and 0.3% MMTS. Resuspended proteins were processed by SNO-RAC as described above.

Glucose uptake measurement—In vitro glucose uptake measurement was performed as previously described [68]. Naïve $SCAN^{+/+}$ and $SCAN^{-/-}$ mice (5 male and 5 female) per group were euthanized by isoflurane anesthesia. Soleus muscles were dissected tendon-to-tendon and rapidly rinsed in ice-cold 1X Krebs–Henseleit buffer. Muscles were recovered in vials including the recovery buffer (1X Krebs–Henseleit buffer, 0.1% BSA, 2 mM sodium pyruvate, 32 mM mannitol, 8 mM glucose supplemented with human-effective insulin dose (12 nM) or without insulin (basal)), shaken at 45 revolutions per minute while continuously gassed (95% O_2–5% CO_2) in a heated water bath (35°C) for 60 minutes. Muscles were subsequently washed twice for 10 minutes with at 35°C for 10 minutes in washing buffer (1X Krebs–Henseleit buffer, 0.1% BSA, 2mM sodium pyruvate and 32 mM Mannitol).

Muscles were transferred to a vial containing 5 ml incubation buffer (1X Krebs–Henseleit buffer, 0.1% BSA, 2 mM sodium pyruvate, 32 mM mannitol, 4 mM 2-deoxyglucose, 2 μCi/ml ^{3}H-2-deoxyglucose, and 0.3 μCi/ml ^{14}C-mannitol). Separate incubations were performed with insulin (12 nM) or without insulin (basal). Vials were shaken at 45 revolutions per minute while continuously gassed (95% O_2–5% CO_2) in a heated water bath (35°C) for 20 minutes. Following this step, muscles were rinsed quickly in 1X Krebs–Henseleit buffer once and dried on filter paper and weighed. Muscle was digested with 1:10 (1 mg/10 μl) 1 M NaOH at 60°C for 1 hour. The samples were centrifuged 15,000 × g for 15 minutes at 4°C. Supernatants (150 μl) were transferred to new tubes and neutralized with 150 μl of 1M HCl. Fifty μl of each neutralized sample was placed in a scintillation vial and the ^{3}H and ^{14}C counts determined in a scintillation counter (PerkinElmer). Extracellular volume was calculated using disintegrations per minute (DPM) of the ^{14}C-mannitol, which is not membrane permeant. Intracellular 2-DG levels were then determined after accounting for ^{3}H DPM in the extracellular space, and 2-DG uptake rates were expressed as nmol 2-DG/100 mg muscle/20 minutes.

Intraperitoneal glucose tolerance test (IPGTT), intraperitoneal insulin tolerance test (IPITT) and acute hypoglycemia—IPGTT and IPITT were performed according to the standard protocol of the International Mouse Phenotyping Consortium (https://www.mousephenotype.org). Mice were fasted for 16 hours for IPGTT or 5 hours for IPITT in clean cages with no food or feces in the bedding, in the standard light–dark cycle and with free access to water. Blood was collected from the tail tip directly onto a glucose test strip and read immediately using a calibrated glucometer. For IPGTT, glucose was injected i.p. at 2 g of glucose/kg of body weight. Blood drawn from sequential tail tip cuts was used to measure glucose at 15, 30, 60, 90 and 120 min after glucose injection. For IPITT, insulin was injected i.p at 1 unit insulin/kg of body weight. Glucose levels in tail tip blood were measured at 15, 30, 60, 90 and 120 min after insulin injection. Insulin-induced acute hypoglycemia (“severe” ITT) in mice was produced according to a published protocol [69]. Insulin (2.5 units/kg body weight) was injected i.p. into 3 h-fasted mice, producing blood glucose <40 mg/dl when measured at 90 min after injection and without leading to unconsciousness, seizures, or death. Blood glucose was measured before insulin injection and after 30, 90, 120,180 and 240 min via tail tip bleed.

Insulin, bilirubin, free hemin, and blood tests—Blood (50 μl) was collected from the mouse facial vein. To measure insulin, bilirubin and free hemin in serum, blood was placed in BD Microtainer tubes with Serum Separator, and centrifuged at 4°C at 2000 × *g* for 10 min to obtain serum. Insulin concentration was measured following the protocol of Ultra Sensitive Mouse Insulin ELISA Kit (Crystal Chem). Mice were fasted for 5 hours prior to basal insulin measurement. Hematology analyses were performed using HESKA HemaTrue System. Blood was placed in heparin-treated 1.5ml microtube. Twenty μl blood was used for measurement of 17 parameters including total red blood cell count, total white blood cell count, total platelet count, hemoglobin concentration, lymphocyte percentage, mid-sized cells (e.g., monocytes) percentage, and granulocyte percentage.

Insulin treatment—For L6 cell treatment, L6 cells at 50–70% confluence on 10 cm plates were starved in DMEM medium (+5% BSA) for 16 hours. Human insulin was added into medium to 100 nM final. Following 10-minute insulin treatment, cells were washed three times using warm 1X PBS, and complete DMEM medium (+10% FBS and 1% Pen-Strep) was added. L6 cells were collected at 1, 30, 60, 120 and 240 minutes after media change and stored −80°C. For mouse treatment, human insulin (1 U/kg body weight) was intraperitoneally injected into mice that had been fasted for five hours. After 30 or 60 minutes, mice were euthanized by isoflurane anesthesia. Skeletal muscle (lateral gastrocnemius) was collected and quickly frozen in liquid nitrogen.

iTRAQ-Coupled SNO-RAC—iTRAQ-Coupled SNO-RAC was carried out as described previously [5]. HEK-BLVRB$^{-/-}$ and HEK-BLVRB$^{+/+}$ (control) lysates were prepared, and SNO-RAC (4 mg of protein per sample) was carried out as described above. SDS/PAGE gels were Coomassie-blue stained, and lanes were separated into eight segments top-to-bottom and collected in two 1.5 ml tubes. Five hundred μl of 50% acetonitrile (ACN)/50% 100 mM ammonium bicarbonate was used to wash gel bands for more than 5 hours while vortexing. After removal of washing buffer, 400 μl of 100% acetonitrile was added to gel pieces and vortexed for 10 min. After removal of ACN, gel pieces were dried in a speed vacuum dryer for 10 min. Two hundred μl of 10 mM dithiothreitol (DTT) was added to dry gel pieces and vortexed for 45 min. After removal of DTT buffer, 200 μl of 55 mM iodoacetamide (IAA) was added to the gel pieces and incubated for 45 min in the dark. After removal of IAA buffer, 400 μl of 1x iTRAQ dissolution solution and 400 μl ACN were used to wash the gel pieces twice. Gel pieces were dried for 10 min in a speed vacuum dryer. 500 ng trypsin in 150 μl 1x iTRAQ buffer was added to dried gel pieces on ice for 30 mins to rehydrate, and then incubated overnight at 37°C. Supernatant from the digested protein solution was transferred to a 1.5 ml tube using gel-loading tips. 200 μl extraction buffer (60% ACN/5% formic acid) were added to gel pieces, vortexed for 30 min, and sonicated for 15 min. The supernatant containing peptide extracts was transferred to the same 1.5 ml tube, and extractions were repeated two more times. The final digested solution pool was dried completely in a speed vacuum dryer.

iTRAQ labeling was performed according to the instructions of iTRAQ Reagents - 4plex Applications Kit. Briefly, 30 μl of iTRAQ dissolution buffer (10x) was added to each sample tube (pH > 7), and then one iTraq labeling reagent (mass 114, 115, 116 or 117) was added to individual sample tubes. Reactions were incubated for more than 5 hours at room temperature with vortexing to ensure complete labeling. The four labeled samples were mixed together and dried. One hundred sixty μl of 5% ACN containing 0.5% TFA was added to the labeled sample mix, and the solution cleaned using C18 ziptips. Briefly, C18 tips were wetted 5 times with 20 μl of 50% ACN, and equilibrated with 100 μl of 5% ACN containing 0.5% TFA. Samples were then loaded to the tip by drawing and expelling 50 cycles to ensure complete binding. The tips were then washed with 20 μl of 5% ACN containing 0.5% TFA 10 times. Peptides were eluted from tips in 3× 20 μl of 60% ACN containing 0.1% formic acid, and eluates combined and dried for LC-MS/MS Analysis.

LC-MS/MS Analysis—Digested peptides were separated by UPLC (Waters, Milford, MA) with a Nano-ACQUITY UPLC BEH300 C18 column. Separated peptides were continuously injected into an Orbitrap Elite hybrid mass spectrometer (Thermo Finnigan, San Jose, CA) by a nanospray emitter (10 μm, New Objective). Peptides were eluted using a linear gradient using mobile phase A (0.1% formic acid in water) and B (100% acetonitrile) was used at a flow rate of 0.3 μl/min, starting with 1% mobile phase B and increasing to 40% B at 65 min for protein interaction identification, or increasing to 40% B at 130 min for iTRAQ experiments. All mass spectrometry data were acquired in positive ion mode. For protein interaction identification, a full MS scan (m/z 350–1800) at resolution of 120,000 was conducted, twenty MS2 scans (m/z 350–1800) were selected using the twenty most intense peptide peaks of full MS scans. CID cleavage mode was performed at normalized collision energy of 35%. For iTRAQ experiments, a full MS scan (m/z 300–1800) at resolution of 120,000 was conducted, and ten MS2 scans (m/z 100–1600) were activated from the five most intense peptide peaks of full MS scans. CID and HCD cleavage modes were performed alternatively of the same peptides selected from full MS scans. MS2 resolution of HCD is 15,000. Bioinformatic software MassMatrix was used to search MS data against a database composed of sequences of mouse proteins from Uniprot and their reversed sequences as a decoy database. Modifications including oxidation of methionine and labeling of cysteine (IA modifications) were selected as variable modifications in searching. For iTRAQ labeling searching, MS tag of N terminus, Lys and/or Tyr were selected as variable modification to test labeling efficiency and fixed modification for iTRAQ quantitation analysis. Trypsin was selected as the in-silico enzyme to cleave proteins after Lys and Arg. Precursor ion searching was within 10 ppm mass accuracy and product ions within 0.8 Da for CID cleavage mode and 0.02 Da for HCD cleavage mode. 95% confidence interval was required for protein identification.

Immunoprecipitation—To investigate the interaction of SCAN and IRS1, Myc-SCAN and IRS1-Flag were co-expressed in HEK293 cells. To investigate the effect of insulin stimulation, disruption of SNO-CoA binding, mutation of SNO site C109/188 and of SCoR, Myc-SCAN, Myc-SCAN-QTG/NAA or Myc-SCAN-C109/188R were co-expressed with INSR-Flag in parental or SCoR-knockout HEK cells or L6 cells. HEK cells or L6 cells were treated with NO donor DPTA (200μM) for 20 hours as required. Anti-rabbit C-Myc Agarose Affinity Gel (Sigma) was used for immunoprecipitation. To investigate the interaction of endogenous SCAN with HO2 or INSR, 10 μg of BLVRB Rabbit monoclonal antibody (Sino Biological) was incubated with 50 μl of Protein G Sepharose (GE) (1:1 slurry) at 4°C overnight, then washed with NETN buffer (150 mM NaCl, 20 mM Tris-Cl (pH 8.0), 0.5 mM EDTA, 0.5% (v/v) Nonidet P-40) three times to prepare for immunoprecipitation. HEK cells or L6 cells were homogenized in EBC lysis buffer (120 mM NaCl, 20 mM Tris-Cl (pH 8.0), 0.5 mM EDTA, 0.5% (v/v) NP-40, 1 mM PMSF and protease inhibitor cocktail). After centrifugation (20,000 × g, 4°C, 20 min, ×2), 2 ml (2 mg/ml) supernatant was pre-cleared by incubation with 50 μl Protein G Sepharose (1:1 slurry) for 1 hour at 4 °C. After spinning at 1000 × g for 1 min, the supernatant was transferred into new tubes and incubated with 50 μl anti BLVRB antibody-Protein G Sepharose or with anti c-Myc-Agarose (1:1 slurry) for 5 hours at 4°C. Beads were washed by NETN buffer and proteins were eluted with 50 μl 1X SDS loading dye containing 5% 2-mercaptoethanol. Eluted proteins were electrophoresed in

4–20% Criterion Precast Midi Protein Gels (Bio Rad), transferred to PVDF membranes, and membranes were blotted with mouse Flag antibody, HO2 antibody or INSR antibody.

Western blot analysis—Proteins were extracted from cells using sonication in RIPA buffer (Sigma) supplemented with 1 mM PMSF, protease inhibitor cocktail and phosphatase inhibitor cocktail. Muscle samples were ground with a mortar and pestle under liquid nitrogen, then the powder added to RIPA buffer as above, and mechanically homogenized using a bead beater. Extracts were clarified by centrifugation (20,000 × g, 4°C, 20 min, ×2), and protein concentration was determined by bicinchoninic acid assay. The extracts were electrophoresed in 4–20% Criterion Precast Midi Protein Gels and transferred to PVDF membranes. Membranes were incubated overnight at 4°C with primary antibodies, washed with PBS containing 0.1% Tween-20, incubated with HRP-conjugated secondary antibody for 1 hour, washed, and detected by chemiluminescent detection (ECL) using X-ray film developer system (JPI, Filmprocessor) or a digital imager system (Kwikquant). Antibodies employed in western blotting included: rabbit polyclonal rabbit Anti-BLVRB (13151-R009, Sino Biological Inc), mouse monoclonal Anti-HO2 (H00003163, Abnova), rabbit polyclonal Anti-IRS1 (06–248, EMD Millipore), rabbit polyclonal Anti-INSRβ (sc-711, Santa Cruz), rabbit monoclonal Anti-INSRβ (phospho-Y1163,1164) (MA5–15148, Invitrogen), rabbit Anti-IRS1 phospho-Tyr608 (09432, EMD Millipore), rabbit monoclonal Anti-NOS2 (D9A5L, Cell Signaling), rabbit Anti-eNOS (phospho-S1177) (PA597371, Invitrogen), rabbit monoclonal Anti-AKT (C67E7, Cell Signaling), rabbit Anti-AKT (phospho-S473) (9271, Cell Signaling), mouse monoclonal p97 (10R-P104A, Fitzgerald), rabbit monoclonal GAPDH (Ab181602, abcam), rabbit monoclonal Anti-AS160 (MA5–14840, Invitrogen), rabbit Anti-AS160 (phospho-T642) (44–1071G, Invitrogen) and mouse monoclonal FLAG-M2 (F3165, Sigma) (see Key Resources). Protein levels were quantified by semi-quantitative analysis from western blots using ImageJ (NIH).

Identification of SNO site of INSR by mass spectrometry—The pcDNA-INSR-FLAG plasmid (GenScript) was transfected into HEK293 cells using PolyJet. Cells were harvested and lysed in EBC lysis buffer. INSR-FLAG was purified from lysate with anti-FLAG M2 affinity gel (Sigma) and eluted with 100 mM phosphate buffer, pH 7.4 containing 100 μg/mL FLAG peptide (Sigma), 100 μM EDTA and 100 μM DTPA. Purified INSR was subsequently treated with 100 μM freshly prepared SNO-CoA for 20 minutes at room temperature in the dark. Following treatment with SNO-CoA, protein was supplemented with 100 μg bovine serum albumin carrier, mixed with 3 volumes ice cold 100% acetone, and kept at −20°C for 30 minutes. Following cold incubation, the sample was spun at 14000 × g for 15 minutes to precipitate protein. Pelleted protein was washed 3 times with ice cold 70% acetone, air dried, and resuspended in 400 μL of HENS buffer. Unreacted SNO-CoA was removed using Zeba desalting spin columns (Thermo Fisher) preequilibrated with HENS buffer. Following filtration, 1 M MMTS and 25% SDS were added into the protein solution (final 20mM MMTS and 2.5% SDS) and the solution was vortexed. The solution was incubated for 20 minutes at 50°C to block free thiols. Protein was again precipitated with 3 volumes ice cold 100% acetone with incubation for 1 hour at −20°C. Following incubation, precipitated proteins were collected by centrifugation at 10000 × g for 10 minutes at 4°C. Supernatant was removed from precipitated protein pellets, and

pellets allowed to dry at room temperature for 10 minutes. Proteins were resuspended in HENS buffer and labeled with iodoTMT (Thermo Fisher) in the presence of 20 mM sodium ascorbate for 1 hour at room temperature in the dark. Reactions were quenched with 20 mM DTT for 15 minutes at room temperature in the dark. Protein was precipitated with 3 volumes ice cold 100% acetone at −20°C for 1 hour, then centrifuged at 10000 × g for 10 minutes at 4°C. Supernatant was removed, and the protein pellet dried for 10 minutes. Protein was resuspended in HENS buffer and treated with 16.67 mM iodoacetamide for 1 hour at room temperature in the dark. Protein was again precipitated as above, supernatant removed, and protein pellet dried. Precipitated protein was then resuspended in 50 mM ammonium bicarbonate buffer, pH 8.0. Proteins were then serially digested with 25 μg/mg protein using Lys-c (4 hours at 37°C) then 20 μg/mg protein using trypsin overnight at 37°C. Following digestion, samples were acidified with 25 μL of 10% TFA. Peptides were processed through a C18 SPE column and then frozen and lyophilized. Lyophilized peptides were resuspended in TBS and enriched using anti-TMT resin (Thermo Fisher) following the manufacturer's instructions, and subsequently frozen and lyophilized. Samples were resuspended in 5% acetonitrile, 0.1% formic acid and run through a 0.22 μm filter to remove any excess anti-TMT resin. Peptides were then injected into LC-MS/MS system for analysis.

Purification of proteins—The recombinant HO2, SCAN-WT or SCAN-QTG-NAA proteins were purified from BL21-CodonPlus Competent *E. coli* cells (Agilent). Overnight *E. coli* cultures were sub-cultured into 1 L of LB medium at 5%. At OD600 of 0.5, cultures were induced with 100 mM IPTG and grown 4 hours at 28°C. Cultures were centrifuged at 4000 × g for 10 min to harvest the cells. Cell pellets from 1 L cultures were lysed by sonication in 10 mL of PBS buffer containing 1 mM PMSF and protease-inhibitor cocktail. After centrifugation at 14500 × g for 20 min, the supernatant was collected and diluted (up to 30 ml) with PBS buffer containing 1 mM PMSF and protease-inhibitor cocktail. This lysate was incubated with 1 mL of Ni-NTA agarose at 4°C for 1 hour with rotation. The slurry was then poured into an empty PD-10 column (GE Healthcare), and the beads washed with 100 mL of 50 mM NaH_2PO_4, 300 mM NaCl buffer containing 20 mM imidazole. Elution was done with 2 mL of 50 mM NaH_2PO_4, 300 mM NaCl, 250 mM imidazole. Eluate buffer was exchanged with modified Roeder D [(20mM HEPES (pH 7.9), 20% (v/v) glycerol, 0.1M KCL, 0.2mM EDTA)] using a Microcon centrifugal filter device (Millipore).

IRS1-FLAG and INSR-FLAG were purified from HEK cells. Briefly, HEK cells were transfected with pcDNA-Flag-hIRS1 or pcDNA-Flag-hINSR plasmid using PolyJet transfection reagent (SignaGen) per manufacturer's instructions and grown for 48 hours. After 48 hours, cells were harvested in IP wash buffer (as above) supplemented with 0.5% Triton X-100 and protease inhibitor cocktail. Cells were lysed by sonication and lysate clarified by centrifugation at 15000 × g for 15 minutes. Anti-FLAG agarose affinity gel was equilibrated into IP wash buffer, and clarified lysate was applied to anti-FLAG agarose affinity gel. After 4 hours incubation in 4°C, beads were washed 5 times with IP wash buffer. Proteins were eluted in 300μL 1xPBS containing 100 μg/mL 3X FLAG peptide. Protein concentration was determined using BCA.

Tyrosine kinase activity—Tyrosine kinase activity of INSR was measured using InsR Kinase Enzyme System-coupled with ADP-Glo™ Assay (Promega). To purify the INSR-FLAG from HEK cells, the same procedure was used in above "Purification of proteins" except INSR-FLAG complex was eluted in 200μL reaction buffer A (provided in InsR Kinase Enzyme System) containing 100 μg/mL 3X FLAG peptide and 2mM $MnCl_2$. Ten μl (100ng/μl) purified INSR-FLAG complex was treated with control Tris buffer or 500 μM SNO-CoA (5 μl) for 30 min at 37°C. Ten μl AxLtide (substrate, 1mg/ml)+ATP (125 μM) mixture was added into the reaction. After 60 min incubation at 25°C, 25 μl ADP-Glo™ Reagent was added into the reaction. Fifty μl kinase detection reagent was added after 40 min incubation at 25°C, and the luminescence read after 30 min incubation at 25°C in a Promega GloMax Luminometer.

Immunostaining—HEK293 cells were grown in 2 mL culture medium to approximately 50% confluency on cover slips in 6-well plates. For studying insulin stimulation, cells were starved in DMEM medium (+5% BSA) for 16 hours. Human insulin was added into medium to 100 nM final concentration for 10min. Media was aspirated, and 1mL cold 4% PFA in PBS was used to fix cells for 15 min at room temperature. After each incubation step, cells were washed 3x with PBS. Cells were permeabilized with PBS +.05% Triton X100 for 5 min, washed, blocked with 8% BSA in PBS for 20min, washed and incubated with primary antibodies diluted in blocking buffer for 2 hours. Primary antibodies rabbit anti-SCAN (Sino Biological Inc), mouse anti-Cytochrome C (Cell Signaling) and mouse anti-AKR1A1 (Origene TA500740 clone 9F1) were used in immunostaining. After washing, secondary antibodies were added for 2 hours at room temperature. Secondary antibodies used were A11001 (Invitrogen, AF488 anti-mouse IgG at 1:1000) and A11036 (AF568 anti-rabbit IgG at 1:1000). DAPI (Biotium, 5mg/ml) was used to stain nuclei. Samples were washed once again, mounted with Fluoromount G onto slides and imaged with a Nikon Eclipse Ti2 microscope using a 60x objective. TIFF images were processed in FIJI/ImageJ with the JaCoP plugin used to calculate Pearson's and M1/M2 coefficients.

QUANTIFICATION AND STATISTICAL ANALYSIS

Statistics were analyzed using GraphPad Prism 8. Comparisons between continuous characteristics of two subject groups were analyzed with two-tailed Student's t-test. For comparisons among more than two groups, one-way ANOVA with Tukey post hoc or two-way ANOVA with Sidak's multiple comparisons test were used. Simple linear regression was performed in comparing human samples. Bar graphs with the corresponding dot plots were created using GraphPad Prism. Results are presented as mean ± SD, and sample sizes or number of replicates are indicated in individual figure legends.

Supplementary Material

Refer to Web version on PubMed Central for supplementary material.

Acknowledgments

This work was supported by NIH grant R01 DK119506, R01 DK137973, R01 HL157151, P01 HL158507, HL126900 and DK128347 to JSS, as well as R01 DK119506 to HLZ and HL126900 to JDR.

References

1. Shi L, and Tu BP (2015). Acetyl-CoA and the regulation of metabolism: mechanisms and consequences. Curr Opin Cell Biol 33, 125–131. 10.1016/j.ceb.2015.02.003. [PubMed: 25703630]
2. Lee CH, and Chen AF (1982). The Pyridine Nucleotide Coenzyme (Academic Press).
3. Shvedunova M, and Akhtar A (2022). Modulation of cellular processes by histone and non-histone protein acetylation. Nat Rev Mol Cell Biol 23, 329–349. 10.1038/s41580-021-00441-y. [PubMed: 35042977]
4. Trefely S, Lovell CD, Snyder NW, and Wellen KE (2020). Compartmentalised acyl-CoA metabolism and roles in chromatin regulation. Mol Metab 38, 100941. 10.1016/j.molmet.2020.01.005. [PubMed: 32199817]
5. Anand P, Hausladen A, Wang YJ, Zhang GF, Stomberski C, Brunengraber H, Hess DT, and Stamler JS (2014). Identification of S-nitroso-CoA reductases that regulate protein S-nitrosylation. Proc Natl Acad Sci U S A 111, 18572–18577. 10.1073/pnas.1417816112. [PubMed: 25512491]
6. Zhou HL, Zhang R, Anand P, Stomberski CT, Qian Z, Hausladen A, Wang L, Rhee EP, Parikh SM, Karumanchi SA, and Stamler JS (2019). Metabolic reprogramming by the S-nitroso-CoA reductase system protects against kidney injury. Nature 565, 96–100. 10.1038/s41586-018-0749-z. [PubMed: 30487609]
7. Stomberski CT, Zhou HL, Wang L, van den Akker F, and Stamler JS (2019). Molecular recognition of S-nitrosothiol substrate by its cognate protein denitrosylase. J Biol Chem 294, 1568–1578. 10.1074/jbc.RA118.004947. [PubMed: 30538128]
8. Li X, Schmohl F, Qi H, Bennewitz K, Tabler CT, Poschet G, Hell R, Volk N, Poth T, Hausser I, et al. (2020). Regulation of Gluconeogenesis by Aldo-ketoreductase 1a1b in Zebrafish. iScience 23, 101763. 10.1016/j.isci.2020.101763. [PubMed: 33251496]
9. Stomberski CT, Venetos NM, Zhou HL, Qian Z, Collison BR, Field SJ, Premont RT, and Stamler JS (2022). A multienzyme S-nitrosylation cascade regulates cholesterol homeostasis. Cell Rep 41, 111538. 10.1016/j.celrep.2022.111538. [PubMed: 36288700]
10. Hess DT, Matsumoto A, Kim SO, Marshall HE, and Stamler JS (2005). Protein S-nitrosylation: purview and parameters. Nat Rev Mol Cell Biol 6, 150–166. 10.1038/nrm1569. [PubMed: 15688001]
11. Stomberski CT, Hess DT, and Stamler JS (2019). Protein S-Nitrosylation: Determinants of Specificity and Enzymatic Regulation of S-Nitrosothiol-Based Signaling. Antioxid Redox Signal 30, 1331–1351. 10.1089/ars.2017.7403. [PubMed: 29130312]
12. Jia J, Arif A, Terenzi F, Willard B, Plow EF, Hazen SL, and Fox PL (2014). Target-selective protein S-nitrosylation by sequence motif recognition. Cell 159, 623–634. 10.1016/j.cell.2014.09.032. [PubMed: 25417112]
13. Nakamura T, Tu S, Akhtar MW, Sunico CR, Okamoto S, and Lipton SA (2013). Aberrant protein s-nitrosylation in neurodegenerative diseases. Neuron 78, 596–614. 10.1016/j.neuron.2013.05.005. [PubMed: 23719160]
14. Rizza S, and Filomeni G (2020). Exploiting S-nitrosylation for cancer therapy: facts and perspectives. Biochem J 477, 3649–3672. 10.1042/BCJ20200064. [PubMed: 33017470]
15. Schiattarella GG, Altamirano F, Tong D, French KM, Villalobos E, Kim SY, Luo X, Jiang N, May HI, Wang ZV, et al. (2019). Nitrosative stress drives heart failure with preserved ejection fraction. Nature 568, 351–356. 10.1038/s41586-019-1100-z. [PubMed: 30971818]
16. Yang L, Calay ES, Fan J, Arduini A, Kunz RC, Gygi SP, Yalcin A, Fu S, and Hotamisligil GS (2015). METABOLISM. S-Nitrosylation links obesity-associated inflammation to endoplasmic reticulum dysfunction. Science 349, 500–506. 10.1126/science.aaa0079. [PubMed: 26228140]
17. Zhou HL, Premont RT, and Stamler JS (2022). The manifold roles of protein S-nitrosylation in the life of insulin. Nat Rev Endocrinol 18, 111–128. 10.1038/s41574-021-00583-1. [PubMed: 34789923]
18. Caranto JD, and Lancaster KM (2017). Nitric oxide is an obligate bacterial nitrification intermediate produced by hydroxylamine oxidoreductase. Proc Natl Acad Sci U S A 114, 8217–8222. 10.1073/pnas.1704504114. [PubMed: 28716929]

19. Lundberg JO, and Weitzberg E (2022). Nitric oxide signaling in health and disease. Cell 185, 2853–2878. 10.1016/j.cell.2022.06.010. [PubMed: 35931019]
20. Nakamura T, Wang L, Wong CC, Scott FL, Eckelman BP, Han X, Tzitzilonis C, Meng F, Gu Z, Holland EA, et al. (2010). Transnitrosylation of XIAP regulates caspase-dependent neuronal cell death. Mol Cell 39, 184–195. 10.1016/j.molcel.2010.07.002. [PubMed: 20670888]
21. Seth D, Hess DT, Hausladen A, Wang L, Wang YJ, and Stamler JS (2018). A Multiplex Enzymatic Machinery for Cellular Protein S-nitrosylation. Mol Cell 69, 451–464 e456. 10.1016/j.molcel.2017.12.025. [PubMed: 29358078]
22. Pawloski JR, Hess DT, and Stamler JS (2001). Export by red blood cells of nitric oxide bioactivity. Nature 409, 622–626. 10.1038/35054560. [PubMed: 11214321]
23. Stamler JS, Lamas S, and Fang FC (2001). Nitrosylation. the prototypic redox-based signaling mechanism. Cell 106, 675–683. 10.1016/s0092-8674(01)00495-0. [PubMed: 11572774]
24. Stamler JS, and Hess DT (2010). Nascent nitrosylases. Nat Cell Biol 12, 1024–1026. 10.1038/ncb1110-1024. [PubMed: 20972426]
25. Kornberg MD, Sen N, Hara MR, Juluri KR, Nguyen JV, Snowman AM, Law L, Hester LD, and Snyder SH (2010). GAPDH mediates nitrosylation of nuclear proteins. Nat Cell Biol 12, 1094–1100. 10.1038/ncb2114. [PubMed: 20972425]
26. Choudhary C, Kumar C, Gnad F, Nielsen ML, Rehman M, Walther TC, Olsen JV, and Mann M (2009). Lysine acetylation targets protein complexes and co-regulates major cellular functions. Science 325, 834–840. 10.1126/science.1175371. [PubMed: 19608861]
27. Bateman RL, Rauh D, Tavshanjian B, and Shokat KM (2008). Human carbonyl reductase 1 is an S-nitrosoglutathione reductase. J Biol Chem 283, 35756–35762. 10.1074/jbc.M807125200. [PubMed: 18826943]
28. O'Brien L, Hosick PA, John K, Stec DE, and Hinds TD Jr. (2015). Biliverdin reductase isozymes in metabolism. Trends Endocrinol Metab 26, 212–220. 10.1016/j.tem.2015.02.001. [PubMed: 25726384]
29. Yamaguchi T, Komoda Y, and Nakajima H (1994). Biliverdin-IX alpha reductase and biliverdin-IX beta reductase from human liver. Purification and characterization. J Biol Chem 269, 24343–24348. [PubMed: 7929092]
30. Shalloe F, Elliott G, Ennis O, and Mantle TJ (1996). Evidence that biliverdin-IX beta reductase and flavin reductase are identical. Biochem J 316 (Pt 2), 385–387. 10.1042/bj3160385. [PubMed: 8687377]
31. Paukovich N, Xue M, Elder JR, Redzic JS, Blue A, Pike H, Miller BG, Pitts TM, Pollock DD, Hansen K, et al. (2018). Biliverdin Reductase B Dynamics Are Coupled to Coenzyme Binding. J Mol Biol 430, 3234–3250. 10.1016/j.jmb.2018.06.015. [PubMed: 29932944]
32. Maines MD (2001). Overview of heme degradation pathway. Curr Protoc Toxicol Chapter 9, Unit 9 1. 10.1002/0471140856.tx0901s00.
33. Pereira PJ, Macedo-Ribeiro S, Parraga A, Perez-Luque R, Cunningham O, Darcy K, Mantle TJ, and Coll M (2001). Structure of human biliverdin IXbeta reductase, an early fetal bilirubin IXbeta producing enzyme. Nat Struct Biol 8, 215–220. 10.1038/84948. [PubMed: 11224564]
34. Tao R, Zhao Y, Chu H, Wang A, Zhu J, Chen X, Zou Y, Shi M, Liu R, Su N, et al. (2017). Genetically encoded fluorescent sensors reveal dynamic regulation of NADPH metabolism. Nat Methods 14, 720–728. 10.1038/nmeth.4306. [PubMed: 28581494]
35. Sallin O, Reymond L, Gondrand C, Raith F, Koch B, and Johnsson K (2018). Semisynthetic biosensors for mapping cellular concentrations of nicotinamide adenine dinucleotides. Elife 7. 10.7554/eLife.32638.
36. Nesbitt NM, Malone LE, Liu Z, Jares A, Gnatenko DV, Ma Y, Zhu W, and Bahou WF (2021). Divergent erythroid megakaryocyte fates in Blvrb-deficient mice establish non-overlapping cytoprotective functions during stress hematopoiesis. Free Radic Biol Med 164, 164–174. 10.1016/j.freeradbiomed.2020.12.015. [PubMed: 33359909]
37. Gibbs PE, Lerner-Marmarosh N, Poulin A, Farah E, and Maines MD (2014). Human biliverdin reductase-based peptides activate and inhibit glucose uptake through direct interaction with the kinase domain of insulin receptor. FASEB J 28, 2478–2491. 10.1096/fj.13-247015. [PubMed: 24568842]

38. Carvalho-Filho MA, Ueno M, Carvalheira JB, Velloso LA, and Saad MJ (2006). Targeted disruption of iNOS prevents LPS-induced S-nitrosation of IRbeta/IRS-1 and Akt and insulin resistance in muscle of mice. Am J Physiol Endocrinol Metab 291, E476–482. 10.1152/ajpendo.00422.2005. [PubMed: 16638822]
39. Carvalho-Filho MA, Ropelle ER, Pauli RJ, Cintra DE, Tsukumo DM, Silveira LR, Curi R, Carvalheira JB, Velloso LA, and Saad MJ (2009). Aspirin attenuates insulin resistance in muscle of diet-induced obese rats by inhibiting inducible nitric oxide synthase production and S-nitrosylation of IRbeta/IRS-1 and Akt. Diabetologia 52, 2425–2434. 10.1007/s00125-009-1498-1. [PubMed: 19730809]
40. Fulton D, Gratton JP, McCabe TJ, Fontana J, Fujio Y, Walsh K, Franke TF, Papapetropoulos A, and Sessa WC (1999). Regulation of endothelium-derived nitric oxide production by the protein kinase Akt. Nature 399, 597–601. 10.1038/21218. [PubMed: 10376602]
41. Cabail MZ, Li S, Lemmon E, Bowen ME, Hubbard SR, and Miller WT (2015). The insulin and IGF1 receptor kinase domains are functional dimers in the activated state. Nat Commun 6, 6406. 10.1038/ncomms7406. [PubMed: 25758790]
42. Switzer CH, Glynn SA, Cheng RY, Ridnour LA, Green JE, Ambs S, and Wink DA (2012). S-nitrosylation of EGFR and Src activates an oncogenic signaling network in human basal-like breast cancer. Mol Cancer Res 10, 1203–1215. 10.1158/1541-7786.MCR-12-0124. [PubMed: 22878588]
43. Okada K, and Zhu BT (2017). S-nitrosylation of the IGF-1 receptor disrupts the cell proliferative action of IGF-1. Biochem Biophys Res Commun 491, 870–875. 10.1016/j.bbrc.2017.06.177. [PubMed: 28709872]
44. Murillo-Carretero M, Torroglosa A, Castro C, Villalobo A, and Estrada C (2009). S-Nitrosylation of the epidermal growth factor receptor: a regulatory mechanism of receptor tyrosine kinase activity. Free Radic Biol Med 46, 471–479. 10.1016/j.freeradbiomed.2008.10.048. [PubMed: 19056486]
45. Yang H, Oh CK, Amal H, Wishnok JS, Lewis S, Schahrer E, Trudler D, Nakamura T, Tannenbaum SR, and Lipton SA (2022). Mechanistic insight into female predominance in Alzheimer's disease based on aberrant protein S-nitrosylation of C3. Sci Adv 8, eade0764. 10.1126/sciadv.ade0764. [PubMed: 36516243]
46. Li S, Yu K, Wu G, Zhang Q, Wang P, Zheng J, Liu ZX, Wang J, Gao X, and Cheng H (2021). pCysMod: Prediction of Multiple Cysteine Modifications Based on Deep Learning Framework. Front Cell Dev Biol 9, 617366. 10.3389/fcell.2021.617366.
47. Abunimer A, Smith K, Wu TJ, Lam P, Simonyan V, and Mazumder R (2014). Single-nucleotide variations in cardiac arrhythmias: prospects for genomics and proteomics based biomarker discovery and diagnostics. Genes (Basel) 5, 254–269. 10.3390/genes5020254. [PubMed: 24705329]
48. Liu L, Hausladen A, Zeng M, Que L, Heitman J, and Stamler JS (2001). A metabolic enzyme for S-nitrosothiol conserved from bacteria to humans. Nature 410, 490–494. 10.1038/35068596. [PubMed: 11260719]
49. Benhar M, Forrester MT, Hess DT, and Stamler JS (2008). Regulated protein denitrosylation by cytosolic and mitochondrial thioredoxins. Science 320, 1050–1054. 10.1126/science.1158265. [PubMed: 18497292]
50. Tejero J, Shiva S, and Gladwin MT (2019). Sources of Vascular Nitric Oxide and Reactive Oxygen Species and Their Regulation. Physiol Rev 99, 311–379. 10.1152/physrev.00036.2017. [PubMed: 30379623]
51. Hashemy SI, and Holmgren A (2008). Regulation of the catalytic activity and structure of human thioredoxin 1 via oxidation and S-nitrosylation of cysteine residues. J Biol Chem 283, 21890–21898. 10.1074/jbc.M801047200. [PubMed: 18544525]
52. Forrester MT, Thompson JW, Foster MW, Nogueira L, Moseley MA, and Stamler JS (2009). Proteomic analysis of S-nitrosylation and denitrosylation by resin-assisted capture. Nat Biotechnol 27, 557–559. 10.1038/nbt.1545. [PubMed: 19483679]
53. Cho DH, Nakamura T, Fang J, Cieplak P, Godzik A, Gu Z, and Lipton SA (2009). S-nitrosylation of Drp1 mediates beta-amyloid-related mitochondrial fission and neuronal injury. Science 324, 102–105. 10.1126/science.1171091. [PubMed: 19342591]

54. Nesbitt NM, Zheng X, Li Z, Manso JA, Yen WY, Malone LE, Ripoll-Rozada J, Pereira PJB, Mantle TJ, Wang J, and Bahou WF (2018). In silico and crystallographic studies identify key structural features of biliverdin IXbeta reductase inhibitors having nanomolar potency. J Biol Chem 293, 5431–5446. 10.1074/jbc.RA118.001803. [PubMed: 29487133]
55. Wu S, Li Z, Gnatenko DV, Zhang B, Zhao L, Malone LE, Markova N, Mantle TJ, Nesbitt NM, and Bahou WF (2016). BLVRB redox mutation defines heme degradation in a metabolic pathway of enhanced thrombopoiesis in humans. Blood 128, 699–709. 10.1182/blood-2016-02-696997. [PubMed: 27207795]
56. Li Z, Nesbitt NM, Malone LE, Gnatenko DV, Wu S, Wang D, Zhu W, Girnun GD, and Bahou WF (2018). Heme degradation enzyme biliverdin IXbeta reductase is required for stem cell glutamine metabolism. Biochem J 475, 1211–1223. 10.1042/BCJ20180016. [PubMed: 29500232]
57. Gao Z, Ni X, Zheng B, Sun W, Wan W, Liu H, Ni X, Suo T, Li N, Liu H, and Shen S (2022). Biliverdin reductase B impairs cholangiocarcinoma cell motility by inhibiting the Notch/Snail signaling pathway. J Cancer 13, 2159–2170. 10.7150/jca.70323. [PubMed: 35517415]
58. Cunningham O, Gore MG, and Mantle TJ (2000). Initial-rate kinetics of the flavin reductase reaction catalysed by human biliverdin-IXbeta reductase (BVR-B). Biochem J 345 Pt 2, 393–399. [PubMed: 10620517]
59. Lerner-Marmarosh N, Shen J, Torno MD, Kravets A, Hu Z, and Maines MD (2005). Human biliverdin reductase: a member of the insulin receptor substrate family with serine/threonine/tyrosine kinase activity. Proc Natl Acad Sci U S A 102, 7109–7114. 10.1073/pnas.0502173102. [PubMed: 15870194]
60. Hinds TD Jr., Burns KA, Hosick PA, McBeth L, Nestor-Kalinoski A, Drummond HA, AlAmodi AA, Hankins MW, Vanden Heuvel JP, and Stec DE (2016). Biliverdin Reductase A Attenuates Hepatic Steatosis by Inhibition of Glycogen Synthase Kinase (GSK) 3beta Phosphorylation of Serine 73 of Peroxisome Proliferator-activated Receptor (PPAR) alpha. J Biol Chem 291, 25179–25191. 10.1074/jbc.M116.731703. [PubMed: 27738106]
61. Duplain H, Burcelin R, Sartori C, Cook S, Egli M, Lepori M, Vollenweider P, Pedrazzini T, Nicod P, Thorens B, and Scherrer U (2001). Insulin resistance, hyperlipidemia, and hypertension in mice lacking endothelial nitric oxide synthase. Circulation 104, 342–345. 10.1161/01.cir.104.3.342. [PubMed: 11457755]
62. Kashyap SR, Roman LJ, Lamont J, Masters BS, Bajaj M, Suraamornkul S, Belfort R, Berria R, Kellogg DL Jr., Liu Y, and DeFronzo RA (2005). Insulin resistance is associated with impaired nitric oxide synthase activity in skeletal muscle of type 2 diabetic subjects. J Clin Endocrinol Metab 90, 1100–1105. 10.1210/jc.2004-0745. [PubMed: 15562034]
63. Perreault M, and Marette A (2001). Targeted disruption of inducible nitric oxide synthase protects against obesity-linked insulin resistance in muscle. Nat Med 7, 1138–1143. 10.1038/nm1001-1138. [PubMed: 11590438]
64. Sugita H, Kaneki M, Tokunaga E, Sugita M, Koike C, Yasuhara S, Tompkins RG, and Martyn JA (2002). Inducible nitric oxide synthase plays a role in LPS-induced hyperglycemia and insulin resistance. Am J Physiol Endocrinol Metab 282, E386–394. 10.1152/ajpendo.00087.2001. [PubMed: 11788371]
65. Stamler JS, Singel DJ, and Loscalzo J (1992). Biochemistry of nitric oxide and its redox-activated forms. Science 258, 1898–1902. 10.1126/science.1281928. [PubMed: 1281928]
66. Lemmon MA, and Schlessinger J (2010). Cell signaling by receptor tyrosine kinases. Cell 141, 1117–1134. 10.1016/j.cell.2010.06.011. [PubMed: 20602996]
67. Skarnes WC, Rosen B, West AP, Koutsourakis M, Bushell W, Iyer V, Mujica AO, Thomas M, Harrow J, Cox T, et al. (2011). A conditional knockout resource for the genome-wide study of mouse gene function. Nature 474, 337–342. 10.1038/nature10163. [PubMed: 21677750]
68. Ching JK, Spears LD, Armon JL, Renth AL, Andrisse S, Collins R.L.t., and Fisher JS (2013). Impaired insulin-stimulated glucose transport in ATM-deficient mouse skeletal muscle. Appl Physiol Nutr Metab 38, 589–596. 10.1139/apnm-2012-0175. [PubMed: 23724874]
69. Poplawski MM, Mastaitis JW, and Mobbs CV (2011). Naloxone, but not valsartan, preserves responses to hypoglycemia after antecedent hypoglycemia: role of metabolic reprogramming in counterregulatory failure. Diabetes 60, 39–46. 10.2337/db10-0326. [PubMed: 20811039]

70. Ozawa K, Whalen EJ, Nelson CD, Mu Y, Hess DT, Lefkowitz RJ, and Stamler JS (2008). S-nitrosylation of beta-arrestin regulates beta-adrenergic receptor trafficking. Mol Cell 31, 395–405. 10.1016/j.molcel.2008.05.024. [PubMed: 18691971]

Bullet points

1. SCAN catalyzes protein S-nitrosylation using S-nitroso-CoA as a cofactor
2. S-nitrosylation of insulin receptor and IRS1 by SCAN regulates insulin signaling
3. Hypernitrosylation of INSR and IRS1 by SCAN causes diabetes
4. SCAN expression correlates with human BMI and INSR S-nitrosylation

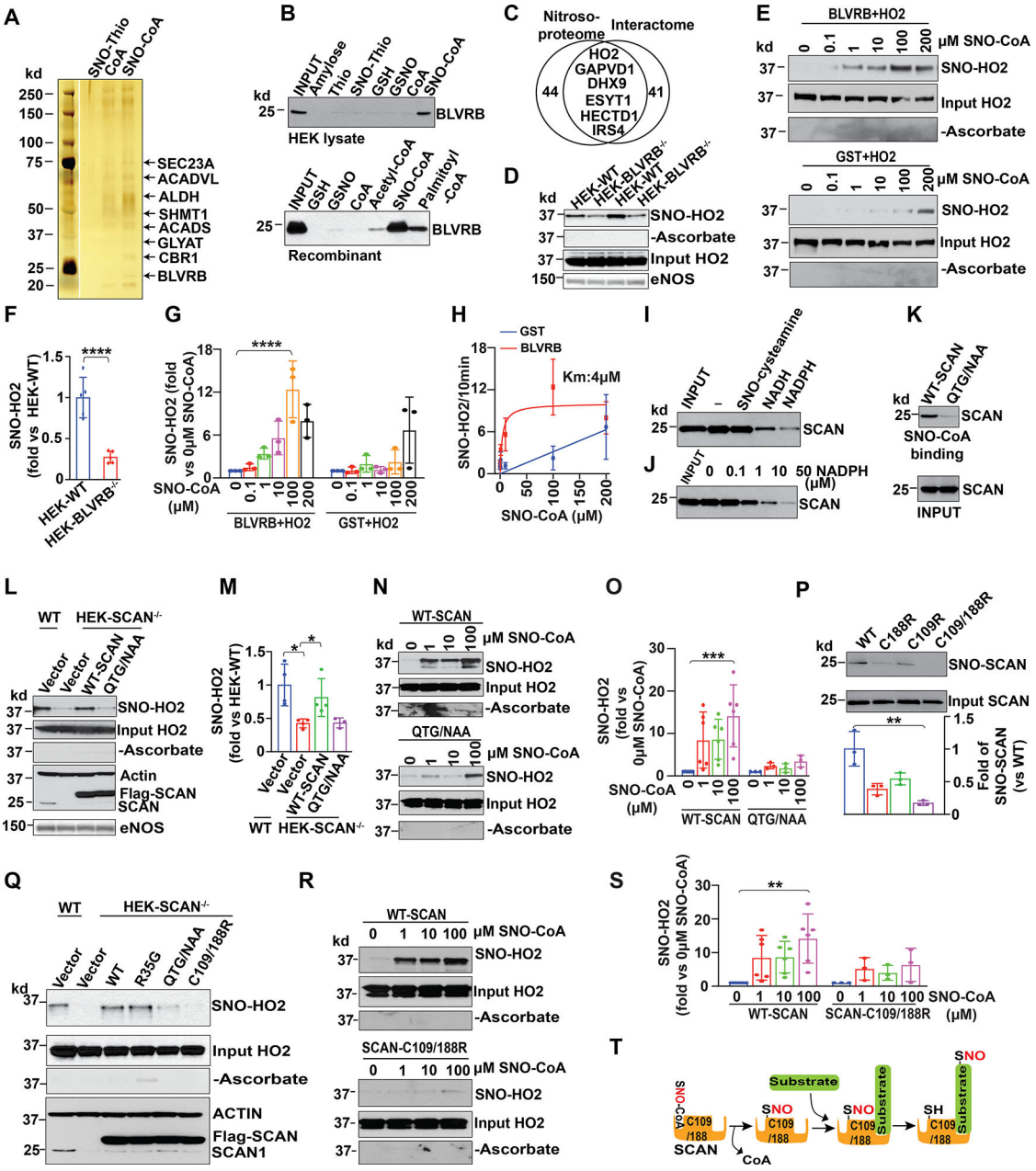

Figure 1. Identification and characterization of a SNO-CoA-Assisted Nitrosyltransferase (SCAN).

(A) Purification of SNO-CoA-binding proteins from bovine liver using SNO-CoA-resin. SNO-thiopropyl- and CoA-resin were used as controls. Eight protein bands identified (including BLVRB) on silver-stained SDS-PAGE gel are indicated by gene name and arrows; n=3. (B) Interaction of SNO-CoA resin with endogenous BLVRB in HEK cell lysate (upper) or with recombinant BLVRB (lower), detected by Western blot. Other resins (amylose resin, thiopropyl Sepharose 6B, SNO-thiopropyl Sepharose 6B, glutathione (GSH)-agarose, glutathione-SNO (GSNO)–Sepharose 4B, CoA–agarose, Acetyl-CoA–agarose and Palmitoyl-Coenzyme A–agarose) were used as controls; n=2. (C) Proteins found in both the BLVRB-dependent nitrosoproteome and the BLVRB cytosolic interactome.

(D) Endogenous S-nitrosylation of HO2 (SNO-HO2) in untargeted HEK cells (HEK-WT) and BLVRB-knockout HEK cells (HEK-BLVRB$^{-/-}$), each expressing eNOS. Results are from two independent cell lines. (E) *In vitro* S-nitrosylation of HO2 by BLVRB in the presence of increasing amounts of SNO-CoA. GST (Glutathione S-transferase) is used as control. (F&G) Quantification of SNO-HO2 (from D, N=4) and (from E, n=3). SNO-HO2 level is normalized to expression of HO2 (input). (H) Enzymatic activity of BLVRB to S-nitrosylate HO2; n=3. (I&J) Competition for SCAN binding to SNO-CoA resin by a fixed dose (50μM) of SNO-cysteamine, NADH or NADPH (I); and by varying amounts of NADPH (J); n=2. (K) Reduced binding of mutant SCAN (QTG/NAA) to SNO-CoA resin; n=2. (L) Endogenous SNO-HO2 in HEK-WT cells (WT), HEK-SCAN$^{-/-}$ cells, wild-type SCAN-re-expressing HEK cells (WT-SCAN) and mutant SCAN-re-expressing HEK cells (QTG-NAA), respectively, each expressing eNOS. (M) Quantification of SNO-HO2 levels in L; n=4. (N) S-nitrosylation of HO2 by recombinant WT-SCAN and SCAN-QTG/NAA protein *in vitro* with increasing SNO-CoA. (O) Quantification of SNO-HO2 in N; n=5. (P) Identification of SNO sites within SCAN. Amount of SNO-SCAN in HEK cell lines overexpressing wild-type SCAN or three mutated SCAN forms (C109R, C188R or C109/188R); n=3. (Q) Amount of SNO-HO2 in HEK-WT versus four HEK-SCAN$^{-/-}$ cell lines overexpressing empty vector, wild-type SCAN (SCAN-WT), SCAN-R35G, SCAN-QTG/NAA and SCAN-C109/188R respectively; n=3. (R) S-nitrosylation of HO2 by recombinant WT-SCAN and SCAN-C109/188R protein *in vitro* with increasing SNO-CoA. (S) Quantification of SNO-HO2 in R; n≥3. (T) Working model of ‘ping-pong’ mechanism utilized by SCAN. The samples of WT-SCAN in Figures O and S are the same. All results are presented as mean ± SD. Two-tailed Student’s t-test was used to detect significance in Fig. 1F. One-way ANOVA with Tukey post hoc was used to detect significance in Fig. 1G, 1M, 1O, 1P and 1S. *, $p<0.05$; **, $p<0.01$; and ****, $p<0.0001$. See also Figures S1 and S2, and Tables S1 and S2.

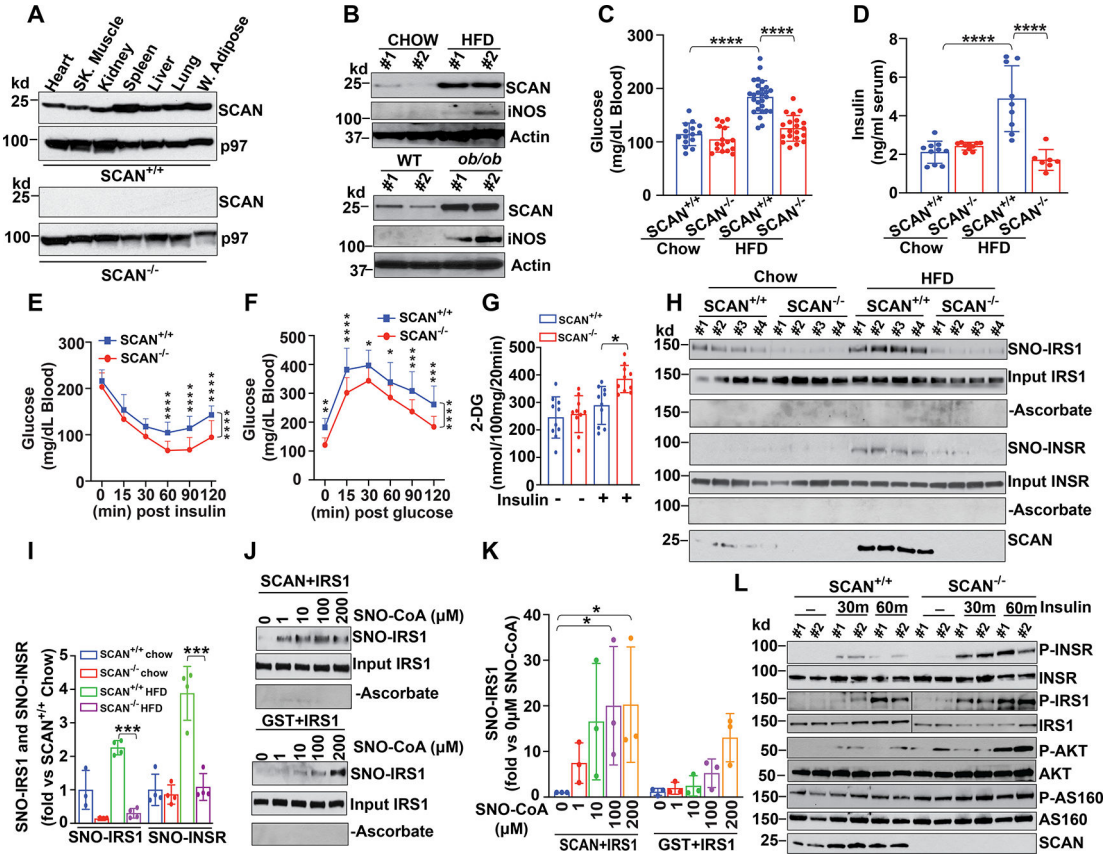

Figure 2. SCAN mediates S-nitrosylation of INSRβ/IRS1 and insulin resistance on high fat diet (HFD).

(A) Expression of SCAN in the indicated organs from wild-type mice ($SCAN^{+/+}$) and SCAN-knockout mice ($SCAN^{-/-}$), vs p97 as loading control; n=2. (B) Expression of SCAN and iNOS in hindlimb skeletal muscle (lateral gastrocnemius) from WT mice fed chow vs HFD for 16-weeks (upper), and from 12-week-old WT vs mutant obese mice (*ob/ob*; lower). Data are shown for two independent mice, and actin is loading control; n=3 mice. (C&D) Blood glucose (C) and plasma insulin levels (D) in chow-fed vs 16-week HFD-fed $SCAN^{+/+}$ and $SCAN^{-/-}$ male mice; n=15–27 overnight-fasted mice in C and n=7–10 5-hour-fasted mice in D, per group. (E) Insulin tolerance test. Blood glucose in 5 hour-fasted 16-week HFD-fed male $SCAN^{+/+}$ and $SCAN^{-/-}$ mice, immediately before and at the indicated time points after injection of human insulin (1U/kg body weight, i.p.); n=22–27 mice per group. (F) Glucose tolerance test. Blood glucose levels in overnight-fasted 16-week HFD-fed male $SCAN^{+/+}$ and $SCAN^{-/-}$ mice, immediately before and at the indicated time points after injection of glucose (2g/kg body weight, i.p.); n=16–23 mice per group. (G) Glucose uptake in *ex vivo* soleus muscles from HFD-fed $SCAN^{+/+}$ and $SCAN^{-/-}$ mice, measured with the non-metabolizable glucose analog 2-deoxyglucose, in the absence or presence of insulin (12 nM); n=10 (5 female and 5 male mice). (H) S-nitrosylation of INSRβ (INSR) and IRS1 in skeletal muscle (lateral gastrocnemius) of 5 hour-fasted chow-fed or HFD-fed $SCAN^{+/+}$ and $SCAN^{-/-}$ mice. (I) Quantification of H; n=4 mice per group. (J) SCAN increases SNO-CoA-induced *in vitro* S-nitrosylation of IRS1 (purified from IRS1-overexpressing HEK cells) compared to GST control (lower). (K) Quantification of J; n=3. (L) Effect of SCAN

on insulin signaling activity markers. Phosphorylation of INSR(pTyr1162), IRS1(pTyr608), AKT(pSer473) and AS160(pThr642) in 5-hour fasted $SCAN^{+/+}$ and $SCAN^{-/-}$ mice, 30 min and 60 min after insulin administration (1U/kg body weight, i.p.), or '-' no insulin administration. Data are from two independent mice at each timepoint, and spliced blots for IRS1/p-IRS1 are indicated. All results are presented as mean ± SD. One-way ANOVA with Tukey post hoc was used to detect significance in Fig. 2C, 2D, 2G, 2I & 2K. ITT and GTT in Fig. 2E and 2F were analyzed by two-way (time × treatment) repeated measures analysis of variance followed by Sidak's multiple comparisons test. *, $p<0.05$; **, $p<0.01$; ***, $p<0.001$; and ****, $p<0.0001$. See also Figures S3 and S4 and Table S4.

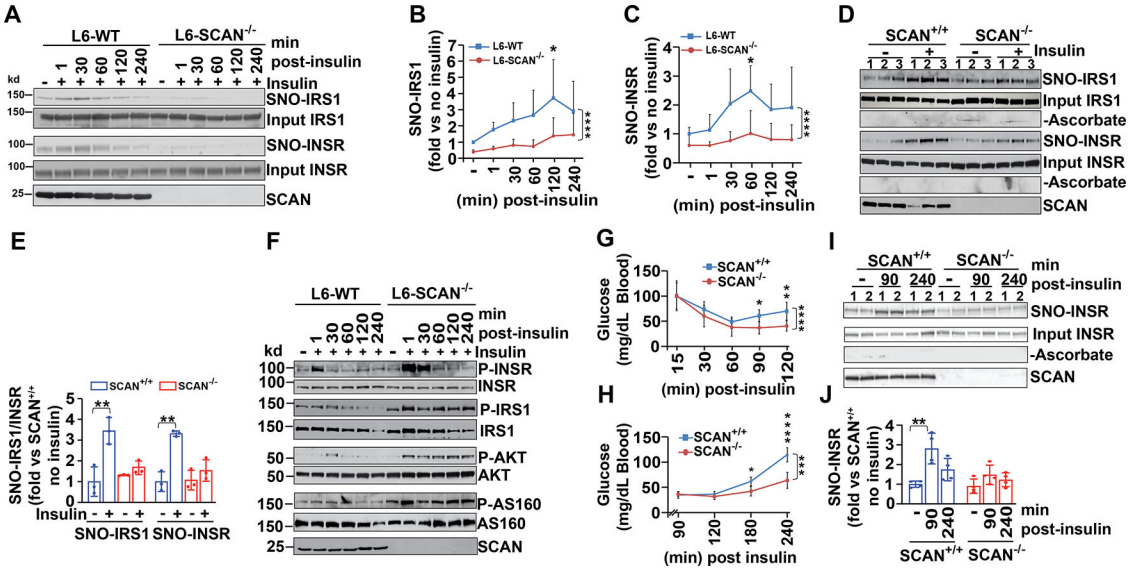

Figure 3. Insulin induces S-nitrosylation of INSRβ/IRS1 to inhibit signal transduction.

(A) SNO-INSRβ and SNO-IRS1 in overnight-starved wild-type L6 cells (L6-WT) and SCAN-knockout L6 cells (L6-SCAN$^{-/-}$) at 1, 30, 60, 120 and 240 min after removal of insulin following 10-minute insulin treatment (100 nM). (B) Quantification of SNO-IRS1 in A, compared to total IRS1; n=3. (C) Quantification of SNO-INSRβ in A, compared to total INSRβ; n=3. (D) SNO-INSRβ and SNO-IRS1 in skeletal muscle (lateral gastrocnemius) from 5-hour fasted SCAN$^{+/+}$ and SCAN$^{-/-}$ mice, 60 min after insulin administration (1U/kg body weight, i.p.) or after no insulin administration (−). (E) Quantification of D; n=3 mice per group. (F) Phosphorylation of INSRβ(pTyr1162), IRS1(pTyr608), AKT(pSer473) and AS160(pThr642) in overnight-starved L6-WT and L6-SCAN$^{-/-}$ cells at 1, 30, 60, 120 and 240 min after removal of insulin, following 10-minute insulin treatment (100 nM); n=4, quantitation shown in Figures S5I–L. (G&H) Normal (G) and severe (H) insulin tolerance test. Blood glucose level in 5-hour fasted chow-fed SCAN$^{+/+}$ and SCAN$^{-/-}$ male mice, immediately before and at the indicated time points after injection of human insulin (1U/kg body weight in panel G; 2.5U/kg body weight in panel H, i.p.); n=10 mice in panels G and H. (I) SNO-INSRβ in skeletal muscle from 2 representative mice during severe insulin challenge as in H. (J) Quantification of I (n=4 mice per condition). All results are presented as mean ± SD. ANOVA with Tukey post hoc was used to detect significance in Fig.3E and 3J. Fig. 3B, 3C, 3G and 3H were analyzed by two-way (time × treatment) repeated measures analysis of variance followed by Sidak's multiple comparisons test. *, p<0.05, **, p<0.01, ***, p<0.001 and ****, p<0.0001. See also Figure S5.

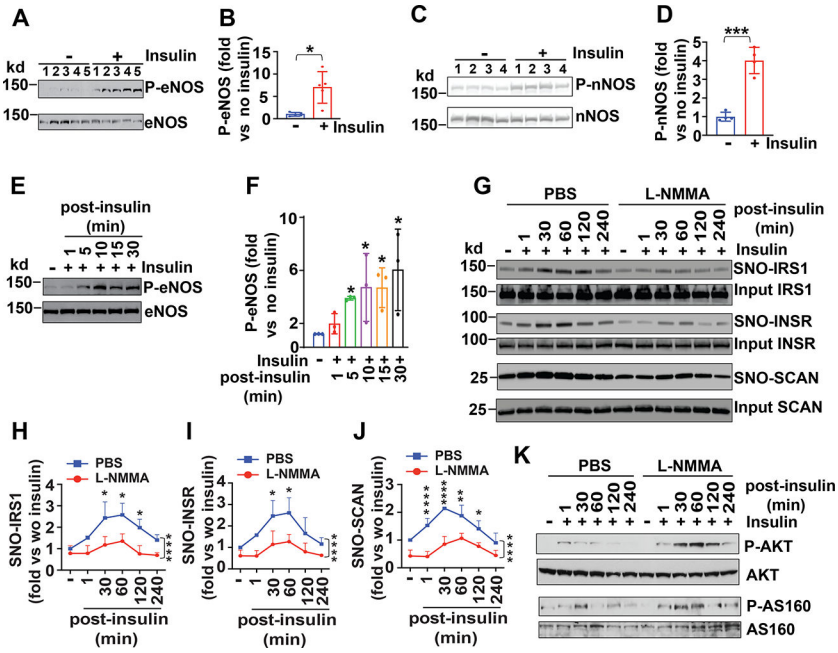

Figure 4. Insulin-stimulated S-nitrosylation of INSRβ/IRS1 is coupled to NOS activity.

(A) Phosphorylation of eNOS(pS1177) in skeletal muscle from 5-hour fasted C57BL/6 mice, 10 min after insulin administration (1U/kg body weight, i.p.). (B) Quantification of A; n=5 mice. (C) Phosphorylation of nNOS(pS1412) in skeletal muscle from 5-hour fasted C57BL/6 mice, 10 min after insulin administration (1U/kg body weight, i.p.). (D) Quantification of C; n=4 mice. (E) Phosphorylation of eNOS(pS1177) in overnight serum-starved L6 cells at the indicated time after removal of insulin, following 10-minute insulin treatment (100 nM). (F) Quantification of E; n=3. (G) Amounts of SNO-INSRβ, SNO-IRS1 and SNO-SCAN in overnight-starved PBS-treated (control) and L-NMMA-treated (100 μM) L6 cells at 1, 30, 60, 120 and 240 min after removal of insulin following 10-minute insulin treatment (100 nM). (H-J) Quantification of SNO-IRS1 (H), SNO-INSRβ (I) and SNO-SCAN (J) from G, respectively; n=3. (K) Phosphorylation of AKT(pSer473) and AS160(pThr642) in PBS-treated (control) and L-NMMA-treated (100 μM) L6 cells at 1, 30, 60, 120 and 240 min after removal of insulin following 10-minute insulin treatment (100 nM); n=3, quantitation shown in Figures S5P–Q. Two-tailed Student's t-test was used to detect significance in Fig. 4B and 4D. One-way ANOVA with Tukey post hoc was used to detect significance in Fig. 4F. Fig. 4H–4J were analyzed by two-way (time × treatment) repeated measures analysis of variance followed by Sidak's multiple comparisons test. *, p<0.05; **, p<0.01; ***, p<0.001; and ****, p<0.0001.

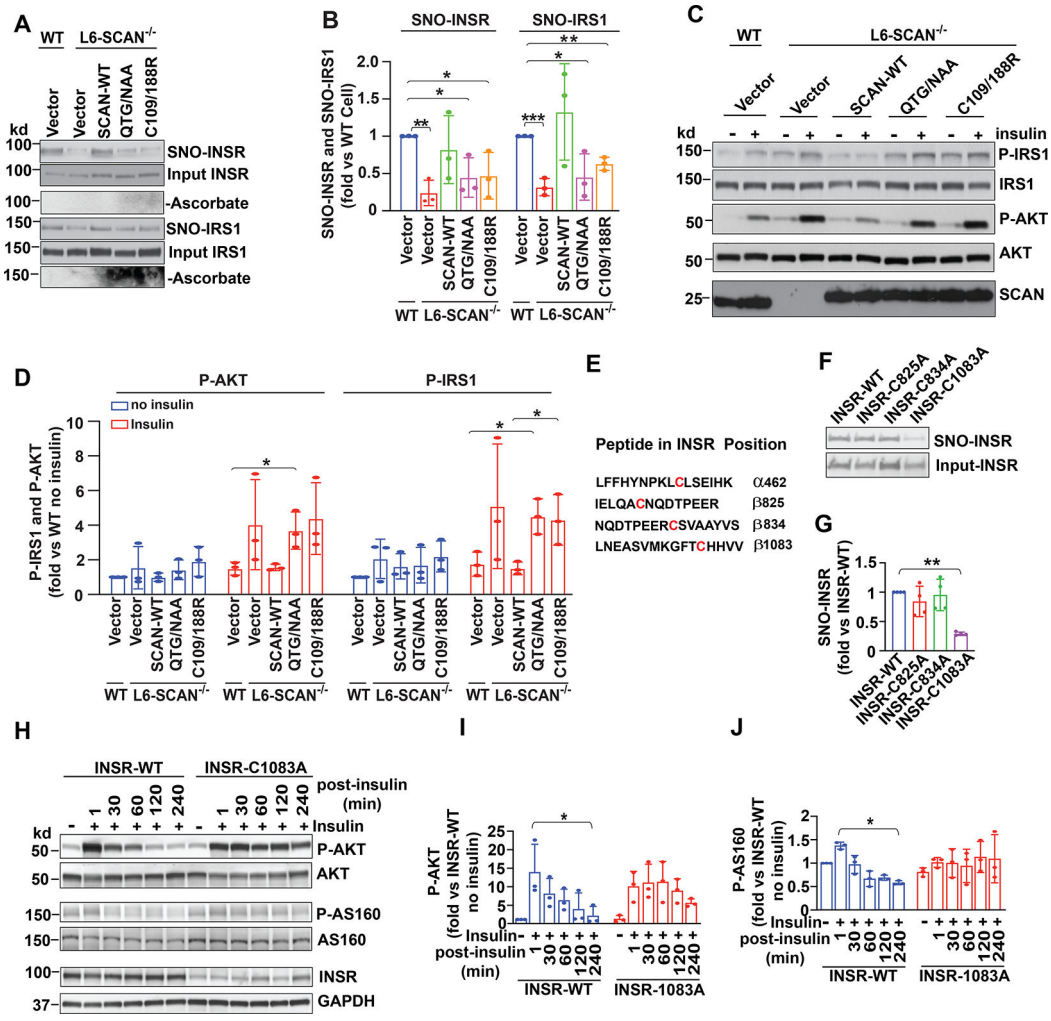

Figure 5. S-nitrosylation of INSRβ by SNO-CoA-dependent SCAN activity regulates insulin signaling.

(A) SNO-INSRβ and SNO-IRS1 in L6-SCAN-WT, L6-SCAN-QTG/NAA and L6-C109/188R cell lines, respectively. (B) Quantification of SNO-INSRβ and SNO-IRS1 in A; n=3. (C) Phosphorylation of IRS1(pTyr608) and AKT(pSer473) in overnight serum-starved L6-SCAN-WT, L6-SCAN-QTG/NAA and L6-C109/188R cell lines, 30 min after a 10-minute insulin treatment (100 nM). (D) Quantification of phosphorylation level of IRS1 and AKT in C; n=3. (E) Four peptides containing single candidate SNO sites (cysteine residues, red) within INSR identified by SNO-RAC-coupled mass spectroscopy. (F) Identification of primary SNO site within INSRβ. SNO-INSRβ with the indicated mutations of candidate SNO sites expressed in HEK cells. (G) Quantification of SNO-INSRβ in F; n=3. (H) Phosphorylation of AKT(pSer473) and AS160(pThr642) in overnight serum-starved INSR-WT and INSR-C1083A expressing L6 cells at 1, 30, 60, 120 and 240 min after removal of insulin, following a 10-minute insulin treatment (100 nM). (I-J) Quantification of phosphorylation of AKT(pSer473) (I) and AS160(pThr642) (J) in H, respectively; n=3. All results are presented as mean ± SD. Two-tailed Student's t-test was used to detect significance in Fig. 5B and 5D. One-way ANOVA with Tukey post hoc was used to detect significance in Fig. 5G, 5I and 5J. *, $p<0.05$ and **, $p<0.01$. See also Figure S6.

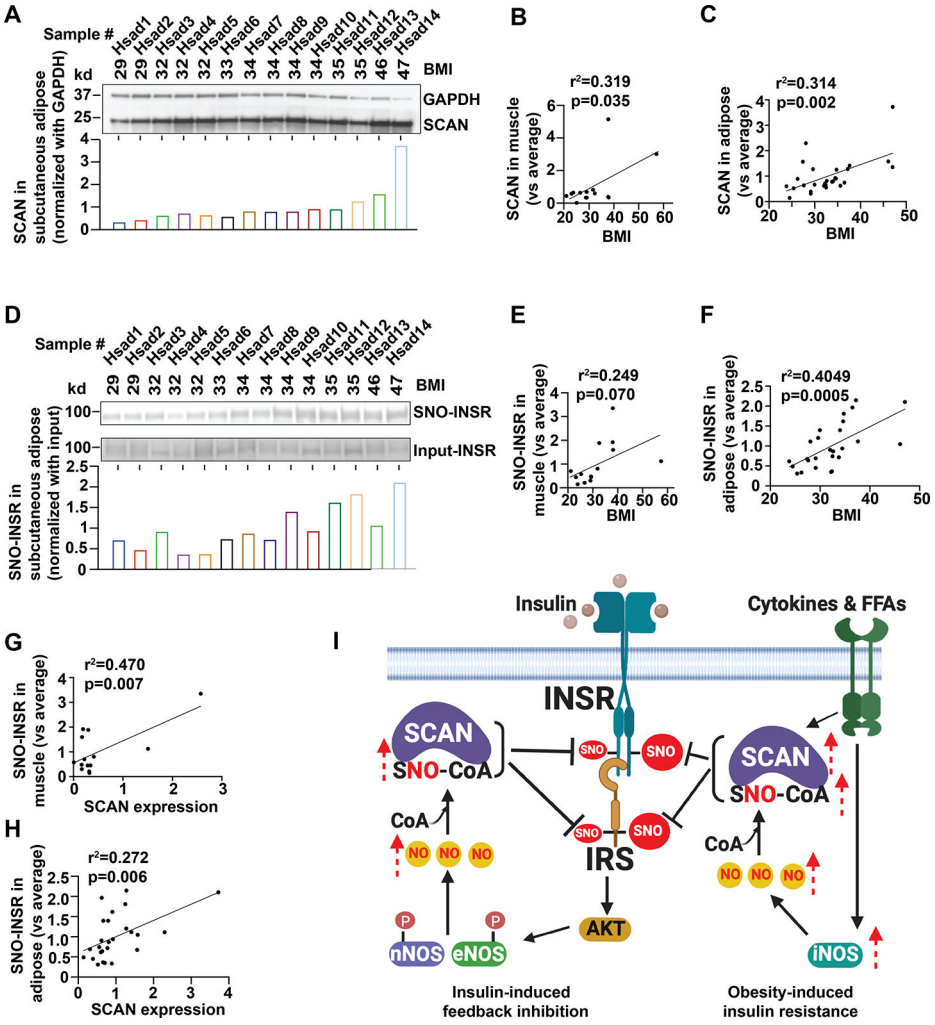

Figure 6. S-nitrosylation of INSRβ is associated with BMI and SCAN expression in human adipose tissue and skeletal muscle.

(A) Expression of SCAN in 14 human subcutaneous adipose samples (Hsad#) with indicated BMI, and quantification (lower panel). GAPDH is used as internal loading control. Expression of SCAN was first normalized with expression of internal control GAPDH, and then versus the average expression level of SCAN in the same group of samples. (B-C) Expression of SCAN in 14 human skeletal muscle samples (B, see Fig. S6E) and 28 human adipose tissue samples (C, see Fig. S6F), plotted against patient BMI. (D) SNO-INSRβ in 14 human subcutaneous adipose samples from patients with the indicated different BMI, and quantification (lower). SNO-INSRβ was first normalized with input of INSRβ, and versus the average SNO-INSRβ level in the same group of samples. (E-F) SNO-INSRβ in 14 human skeletal muscle samples (E, see Fig. S6G) and 26 human adipose tissue samples (F, see Fig. S6H), plotted against patient BMI. (G) SNO-INSRβ in 14 human skeletal muscle samples is plotted against SCAN expression level. (H) SNO-INSRβ in 26 human adipose tissue samples is plotted against SCAN expression level. (I) S-nitrosylation-based inhibition of insulin signaling and insulin resistance. Under healthy conditions, insulin induces S-nitrosylation of INSRβ/IRS1 via eNOS/nNOS-coupled SCAN/SNO-CoA

activity, promoting termination of insulin signaling. In obesity, pro-inflammatory cytokines and free fat acids (FFAs) induce sustained S-nitrosylation of INSRβ/IRS1 through iNOS-coupled SCAN/SNO-CoA activity, leading to insulin resistance. Simple linear regression was performed to identify the relationships among BMI, SCAN expression level, and SNO-INSRβ level (using blot data in A, D and Fig. S6E–H). R-Squared (r^2) and slope significance p values show the goodness of fit of the regression model. See also Figure S6 and Tables S3 and S4.

Key resources table

REAGENT or RESOURCE	SOURCE	IDENTIFIER
Antibodies		
Anti-BLVRB rabbit monoclonal	Sino Biological	Cat# 13151-R009
Anti-HO2 mouse monoclonal	Abnova	Cat# H00003163- M01; RRID:AB_425487
Anti-IRS1 rabbit polyclonal	EMD Millipore	Cat# 06–248, RRID:AB_2127890
Anti-INSR-beta rabbit polyclonal	Santa Cruz	Cat# sc-711, RRID:AB_631835)
Anti-INSR-beta phospho-Y1135,1136,1150,1151 rabbit monoclonal	Invitrogen	Cat# MA5–15148 RRID:AB_10982593
Anti-IRS1 phospho-Y608 rabbit polyclonal	EMD Millipore	Cat# 09–432, RRID:AB_1163457
Anti-NOS1 rabbit monoclonal	Cell Signaling	Cat# 4231 RRID:AB_2152485
Anti-NOS2 rabbit monoclonal	Santa Cruz	Cat# sc-8310 RRID: AB_2152867
Anti-NOS3 rabbit monoclonal	Cell Signaling	Cat#:9572 RRID:AB_329863
Anti-NOS3 phospho-S1177 rabbit polyclonal	ThermoFisher	Cat# PA5–97371, RRID:AB_2809173
Anti-NOS1 phospho-S1417 rabbit polyclonal	Abcam	Cat#ab5583 RRID:AB_304964
Anti-AKT(pan) rabbit monoclonal	Cell Signaling	Cat# 4691, RRID:AB_915783
Anti-AKT phospho-S473 rabbit polyclonal	Cell Signaling	Cat# 9271, RRID:AB_329825
Anti-p97 mouse monoclonal	Fitzgerald Industries	Cat# 10R-P104a, RRID:AB_1287614
Anti-GAPDH mouse monoclonal	Abcam	Cat# ab181602, RRID:AB_2630358
Anti-AS160 rabbit monoclonal	ThermoFisher	Cat# MA5–14840, RRID:AB_10979793
Anti-AS160 phospho-T642 rabbit polyclonal	ThermoFisher	4Cat# 44–1071G, RRID:AB_2533564
Anti-ACADVL	Santa Cruz	Cat#sc-271225 RRID:AB_10609094
Anti-FLAG M2	Sigma-Aldrich	Cat# F3165, RRID:AB_259529
Anti-AKR1A1 mouse monoclonal	Origene	Cat#TA500740 RRID:AB_11128818
Anti-AKR1A1 mouse monoclonal	Santa Cruz	Cat# sc-100500 RRID:AB_1118799
Anti-Histone3 rabbit	Cell Signaling	Cat#9705 RRID:AB_331563
Anti-cytochrome C mouse monoclonal	Cell Signaling	Cat#12963 RRID:AB_2637072
Anti-c-myc mouse monoclonal	R&D system	Cat#MAB3696
Anti-Flag mouse monoclonal	Sigma-Aldrich	Cat#F1804 RRID:AB_262044
Anti-His-Tag	Cell Signaling	Cat#2365 RRID:AB_2115720
Anti-c-myc agarose	Sigma-Aldrich	Cat# A7470, RRID:AB_10109522
Anti-FLAG M2-agarose	Sigma-Aldrich	Cat# A2220, RRID:AB_10063035
Bacterial and virus strains		
BL21-CodonPlus E. coli	Agilent	Cat# 230245
Biological samples		
De-identified human skeletal muscle samples, human visceral adipose samples and human subcutaneous adipose tissue samples	Tissue Resource Core at University Hospitals Cleveland/CWRU	https://cwru.corefacilities.org/service_center/show_external/4499?name=tissue-resource-core
Bovine liver	Rockland Cat# BV-T278	Rockland Cat# BV-T278
Fetal bovine serum (FBS)	Sigma-Aldrich Cat# F4135	Sigma-Aldrich Cat# F4135

REAGENT or RESOURCE	SOURCE	IDENTIFIER
Chemicals, peptides, and recombinant proteins		
Coenzyme A-agarose powder	Sigma-Aldrich	Cat# C7013
Amylose-resin	BioLabs	Cat# E8021S
Activated thiol-Sepharose 4B	GE Healthcare	Cat# 17–0640-01
Thiopropyl-Sepharose 6B	GE Healthcare	Cat# 17–0420-01
Acetyl-CoA-agarose	This study	N/A
Palmitoyl-CoA-agarose	Sigma-Aldrich	Cat# P5297
Glutathione (reduced)-agarose	Invitrogen	Cat# G2879
SNO-modified activated thiol-Sepharose 4B	This study	N/A
SNO-modified coenzyme A (GSNO)-agarose	This study	N/A
Anti-TMT resin	ThermoFisher	Cat# 90060
Protein A/G-Agarose	Thermo Scientific	Cat# 20423
Ni-NTA-agarose	Thermo Scientific	Cat# 88221
3X FLAG peptide	Sigma-Aldrich	Cat# F4799
[3H]-2-deoxyglucose	PerkinElmer	Cat# NET549250UC
[14C]-mannitol	PerkinElmer	Cat# NEC852050UC
Insulin (human)	Sigma-Aldrich	Cat# I9278
PolyJet transfection reagent	SignaGen	Cat# SL100688
DMEM, high glucose	Thermo Scientific	Cat# 11965092
Penecillin/streptomycin	Thermo Scientific	Cat# 15140122
Puromycin	Thermo Scientific	Cat# A1113803
Krebs-Henseleit buffer	Thermo Scientific	Cat# J67795-AP
Sodium pyruvate	Thermo Scientific	Cat# 11360070
Mannitol	Sigma-Aldrich	Cat# M4125
2-deoxyglucose	Sigma-Aldrich	Cat# D8375
DPTA (diethylenetriaminepentaacetic acid)	Cayman Chemical	Cat# 33307
NaNO2	Fluka	Cat# 71759
Bovine serum albumin (BSA)	Sigma-Aldrich	Cat# A2153
Neocuproine	Sigma-Aldrich	Cat# N1501
Protease inhibitor mix	Roche	Cat# 04693132001
Phenylmethylsulfonyl fluoride (PMSF)	Sigma-Aldrich	Cat# P7626
Imidazole	Sigma-Aldrich	Cat# I3386
2-mercaptoethanol	Sigma-Aldrich	Cat# M6250
S-methylmethanethiosulfonate (MMTS)	Sigma-Aldrich	Cat# M9386
Sodium ascorbate	Sigma-Aldrich	Cat# 11140
Critical commercial assays		
QuikChange II Site-Directed Mutagenesis Kit	Agilent	Cat# 200523
Bicinchoninic acid (BCA) protein quantitation kit	ThermoFisher	Cat# 23225
Accu-Chek glucose test strip	Roche	Cat#07299702001

REAGENT or RESOURCE	SOURCE	IDENTIFIER
Ultra Sensitive Mouse Insulin ELISA kit	Crystal Chem	Cat# 90080
Bilirubin assay kit	Sigma-Aldrich	Cat# MAK126
iTRAQ Reagents Multiplex kit	Sigma-Aldrich	Cat# 4352135
iodoTMTsixplex Isobaric Label Reagent Set	ThermoFisher	Cat# 90101
Hemin Assay Kit	BioVison	Cat# K672
InsR Kinase Enzyme System	Promega	Cat#V3901
ADP-Glo™ Kinase Assay	Promega	Cat#V9101
Deposited data		
Raw images for Western blots	This study	doi:10.17632/zz3ktsyjds.1
Experimental models: Cell lines		
HEK293 cells	ATCC	Cat# PTA-4488, RRID:CVCL_0045
Rat L6 cells	ATCC	Cat# CRL-1458, RRID:CVCL_0385
HEK293 SCAN-KO cells	This study	N/A
HEK293 SCAN-KO/SCAN-WT re-expressing cells	This study	N/A
HEK293 SCAN-KO/SCAN-QTG/NAA-expressing cells	This study	N/A
HEK293 SCAN-KO/SCAN-C109/188R-expressing cells	This study	N/A
HEK293-SCoR-KO cells	Stomberski Et al.[9]	N/A
L6 SCAN-KO cells	This study	N/A
L6 SCAN-KO/SCAN-WT re-expressing cells	This study	N/A
L6 SCAN-KO/SCAN-QTG/NAA-expressing cells	This study	N/A
L6 SACN-KO/SCAN-C109/188R-expressing cells	This study	N/A
L6 Insr-KO cells	This study	N/A
L6 Insr-KO/INSR-WT re-expressing cells	This study	N/A
L6 Insr-KO/INSR-C1083S-expressing cells	This study	N/A
Experimental models: Organisms/strains		
$Blvrb^{tm1(KOMP)Wtsi}$ (SCAN-KO) mice	Model Animal Research Center, Nanjing University	RRID:MGI:5756156
B6.Cg-Lep^{ob}/J (ob/ob) mice	Jax.org	Cat# 000632, RRID:IMSR JAX:00 0632
Oligonucleotides		
SCAN-KO genotyping primer Blvrb-FRT-tF1 5'-AGAGTTTGGGTCCTCCCTTTCCT-3'	ThermoFisher	N/A
SCAN-KO genotyping primer Common-En2-R 5'-CCAACTGACCTTGGGCAAGAACAT-3'	ThermoFisher	N/A
rat sgRNA 1 (Blvrb/SCAN) 5'-CCCCTCTGACGGTAACCTGC-3'	GenScript	N/A
rat sgRNA 2 (Blvrb/SCAN) 5'-TCGGTGCCACCGGAAGGACC-3'	GenScript	N/A
rat sgRNA 1 (Insr) 5'-TATCGACTGGTCCCGCATCCTGG-3'	GenScript	N/A
rat sgRNA 2 (Insr) 5'-GCCTGATTATCAACATCCGAGGG-3'	GenScript	N/A
Mutagenesis primers (See Table S5)	GenScript	See Table S5
Recombinant DNA		

REAGENT or RESOURCE	SOURCE	IDENTIFIER
pcDNA3 human IRS1-FLAG	GenScript	Cat# OHu24973
pcDNA3 human INSR-FLAG	Genscript	Cat# OHu24951
pcDNA3.1 vector	ThermoFisher	Cat# V79020
pcDNA3.1 human HO2	This study	N/A
pcDNA3.1 human HO2 C127R mutant	This study	N/A
pcDNA3.1 human HO2 C265R mutant	This study	N/A
pcDNA3.1 human HO2 C282R mutant	This study	N/A
pcDNA3.1 human HO2 1–296	This study	N/A
pcDNA3.1 human HO2 65–316	This study	N/A
pcDNA3.1 human HO2 130–316	This study	N/A
pcDNA3.1 human HO2 195–316	This study	N/A
pcDNA3.1 human SCAN(BLVRB)	This study	N/A
pcDNA3.1 human SCAN QTG-NAA mutant	This study	N/A
pcDNA3.1 human SCAN C109R mutant	This study	N/A
pcDNA3.1 human SCAN C188R mutant	This study	N/A
pcDNA3.1 human SCAN C109/188R mutant	This study	N/A
pcDNA3 human INSR C825A mutant	This study	N/A
pcDNA3 human INSR C834A mutant	This study	N/A
pcDNA3 human INSR C1083A mutant	This study	N/A
pcDNA3 human NOS3 (eNOS)	Ozawa Et al. [70]	N/A
pET21b vector	Sigma-Aldrich	Cat# 69741
pET21b human HO2–6xHis	This study	N/A
pET21b human HO2–6xHis-195–316	This study	N/A
pET21b human SCAN-6xHis	This study	N/A
pET21b human SCAN-6xHis QTG-NAA mutant	This study	N/A
pET21b human SCAN-6xHis C109/188R mutant	This study	N/A
Human BLVRB CRISPR/Cas9 KO plasmid	Santa Cruz Biotechnology	Cat# sc-405988
Human BLVRB HDR plasmid	Santa Cruz Biotechnology	Cat# sc-405988- HDR
Rat eSpCas9-Blvrb targeting plasmid	GenScript	N/A
Rat eSpCas9-Insr targeting plasmid	GenScript	N/A
Software and algorithms		
GraphPad Prism, v8	GraphPad Inc	https://www.graphpad.com/
Other		
High-fat diet for mice (60 kcal% fat diet)	Research Diets, Inc.	D12492
Teklad rodent chow diet	Envigo	P3000